Lithos 204 (2014) 59–72

Contents lists available at ScienceDirect

Lithos

journal homepage: www.elsevier.com/locate/lithos

Origin of two types of rhyolites in the Tarim Large Igneous Province: Consequences of incubation and melting of a mantle plume

Hai-Quan Liu [a,b], Yi-Gang Xu [a,*], Wei Tian [c], Yu-Ting Zhong [a,b], Roland Mundil [d], Xian-Hua Li [e], Yue-Heng Yang [e], Zhen-Yu Luo [a], Shi-Mai Shang-Guan [a,b]

[a] State Key Laboratory of Isotope Geochemistry, Guangzhou Institute of Geochemistry, Chinese Academy of Sciences, Guangzhou 510640, China
[b] University of Chinese Academy of Sciences, Beijing 100049, China
[c] Key Laboratory of Orogenic Belts and Crustal Evolution, MOE, School of Earth and Space Sciences, Peking University, Beijing 100871, China
[d] Berkeley Geochronology Center, 2455 Ridge Road, Berkeley, CA 94709, USA
[e] State Key Laboratory of Lithospheric Evolution, Institute of Geology and Geophysics, Chinese Academy of Sciences, Beijing 100029, China

ARTICLE INFO

Article history:
Received 15 October 2013
Accepted 4 February 2014
Available online 19 February 2014

Keywords:
Rhyolites
Crustal anatexis
Assimilation–fractional crystallization
Mantle plume
Tarim
Large Igneous Province

ABSTRACT

The Early Permian Tarim Large Igneous Province (LIP) in northwestern China contains a large area of silicic volcanics (~48,000 km^2) which are spatially and temporally associated with mafic–ultramafic rocks. In order to understand the behavior of crust above a mantle plume, selected rhyolitic samples are investigated in terms of U–Pb zircon dating, geochemical and isotopic analyses. The Tarim rhyolites have high A/CNK ratios (= molar $Al_2O_3/CaO + Na_2O + K_2O$), $Fe^{\#}$, Ga/Al ratios, concentrations of high field strength elements (HFSEs) such as Zr and Nb, and rare earth elements (REEs), along with high zircon saturation temperatures (872–940 °C), typical of aluminous A-type granitoids. Two contrasting rock types have been recognized. The low Nb–Ta type rhyolites are mainly associated with the first phase of the Tarim flood basalt magmatism at ~290 Ma. They are characterized by negative Nb–Ta anomalies, low $\varepsilon_{Nd}(t)$ and $\varepsilon_{Hf}(t)$ values, and high $^{87}Sr/^{86}Sr(t)$ and $\delta^{18}O_{zircon}$ values, consistent with a derivation from continental crustal source. The high Nb–Ta type rhyolites and their plutonic equivalents are associated with the second episode of Tarim magmatism (283–272 Ma). They are characterized by small negative to positive Nb–Ta anomalies, oceanic island basalt (OIB)-like trace element ratios, low $^{87}Sr/^{86}Sr(t)$ and high $\varepsilon_{Nd}(t)$ and $\varepsilon_{Hf}(t)$ values. These high Nb–Ta rhyolites are best interpreted as hybrid products of crystal fractionation of mafic magmas, coupled with crustal assimilation.

The temporal and compositional evolution of the Tarim rhyolites reflects various extents of thermal and mass exchange between mantle-derived basaltic magma and crustal material above a mantle plume. When the plume head rises to the base of the Tarim craton, it first melts enriched components in the lithospheric mantle (~290 Ma), part of which may have ponded near the crust–mantle boundary and induced crustal anatexis leading to the formation of the low Nb–Ta type rhyolites. At ~280 Ma, large magma chambers and plumbing systems were formed due to increasing magma supply rate during decompression melting of the mantle plume. This led to the formation of a mafic–ultramafic and felsic association of which the high Nb–Ta type rhyolites are a part.

1. Introduction

Large igneous provinces (LIPs) are the most significant output of mantle mafic material at the Earth's surface after basaltic magmas emplaced at mid-ocean ridges (Bryan et al., 2002; Coffin and Eldholm, 1994). Previous studies of LIPs have mostly been focused on mafic–ultramafic rocks and reflect composition of mantle and deep dynamics process (Coffin and Eldholm, 1994). However, significantly less attention has been paid to silicic volcanic rocks in LIPs because they are relatively minor in volume and are poorly exposed/preserved, and this has limited our understanding of the role of crust in the formation of LIPs. Recently, Bryan and his colleagues have summarized the eruption/emplacement and lithological characteristics of silicic magmas in LIPs (Bryan and Ernst, 2008; Bryan et al., 1997, 2002). These papers recognize silicic volcanics as a significant component of LIPs. There are LIPs in which silicic volcanics are minor such as Paraná–Etendeka and North Atlantic LIPs; there are also LIPs in which silicic volcanics are dominant, i.e., Chon Aike, and are known as "Silicic Large Igneous Provinces (SLIPs)" (Bryan, 2007; Bryan et al., 2002). Two mechanisms have been proposed to account for petrogenesis of silicic magmas in LIPs: (1) crustal melting and (2) fractionation of mantle-derived magmas, if any, combined with assimilation of crustal materials. In the first scenario, silicic magmas are partial melting products of mantle-derived

* Corresponding author at: Guangzhou Institute of Geochemistry, Chinese Academy of Sciences, 510640 Wushan, Guangzhou, PR China. Tel.: +86 20 85290109; fax: +86 20 85290261.
E-mail address: yigangxu@gig.ac.cn (Y.-G. Xu).

http://dx.doi.org/10.1016/j.lithos.2014.02.007
0024-4937/

magmas or ancient crustal materials (Bryan et al., 2002; Ewart et al., 2004; Nash et al., 2006). The key factor for large scale partial melting of crust is the "wet components" acquired during previous subduction events (Bryan et al., 2002). In the second case, silicic magmas are formed by fractional crystallization of mantle-derived magmas in which variable extents of crustal material may be involved (Ewart et al., 2004; Xu et al., 2010). Recognizing the role of crust in the genesis of silicic volcanics in LIPs is therefore of great scientific interest.

The early Permian Tarim LIP in northwestern China has recently become a focus of research. Covering an area of more than 250,000 km^2 (Tian et al., 2010; Yang et al., 2006a), it is predominantly composed of basaltic lava flows, mafic–ultramafic layered intrusions/dykes, and spatially and temporally associated felsic volcanic and plutonic rocks. An assimilation–fractional crystallization (AFC) mechanism has previously been proposed to explain the petrogenesis of Early Permian granitoids emplaced in northwestern Tarim (Zhang et al., 2010). However, because of the difference in isotopic composition and the gap in emplacement age between mafic and felsic end-members (Wei et al.,2014) doubt has been cast on this model. This is because, in detail, basalts in the Tarim LIP have negative ε_{Nd} values (-9 to -1) whereas the extrusive/intrusive felsic magmas have mostly higher ε_{Nd} values (-2 – $+4$) (Tian et al., 2010; Wei and Xu, 2011; Wei et al., 2014; Zhang et al., 2010; Zhou et al., 2009). In terms of the AFC model it remains unclear why the granitoids exhibit an isotopically more mantle-like character than the "coeval" basalts.

In addition, a recent compilation of available chronological data has identified two episodes of magmatism in the Tarim LIP (Wei et al., 2014; Xu et al., 2013). The early episode (~290 Ma) is represented by the Keping basalts with negative ε_{Nd}, which are thought to be derived from an enriched lithospheric mantle. The second episode (~280 Ma) is represented by the Bachu dyke swarm and layered mafic–ultramafic intrusions/dykes, with positive ε_{Nd}, which are interpreted as decompression melts from a mantle plume (Wei et al., 2014; Xu et al., 2013). Clearly, the petrogenesis of felsic magmas in the Tarim LIP needs reconsideration, especially in the context of mafic magmatism. In this study, we have carried out zircon U–Pb dating, major and trace elements and Sr–Nd–Hf–O isotopic analyses on a suite of felsic samples collected from outcrops and recovered from drilling holes in Tarim basin. In combination with previously published results, these new data will be used, (a) to discuss the petrogenesis of felsic rocks and to clarify their temporal and spatial relationships with mafic members of the Tarim LIP, and (b) to propose a genetic model to explain the temporal distribution of the Tarim magmatism.

2. Geological background and samples

The Tarim Craton, located in the Xinjiang Uygur Autonomous Region of northwestern China, is one of the three major crustal blocks in China, occupying an area of more than 600,000 km^2. Covered by extensive Cenozoic sediments, the Precambrian basement rocks of Tarim mainly outcrop along the northern (Kuerle region) and southwestern margins (Tiekelike region) (Fig. 1). The oldest basement consists of Neoarchean to early Paleoproterozoic tonalite–trondhjemite–granodiorite (TTG) gneisses and supracrustal rocks (Hu et al., 2000; Long et al., 2010). Precambrian sequences of metasediments are composed of marine sediments, glacial deposits and sedimentary–volcanogenic series distributed along the northern and southwestern margins (Wang et al., 2009; XJBGMR, 1993; Xu et al., 2005). Neoproterozoic granitoids, mainly consisting of gneissic biotite granites, granodiorites and tonalities, intruded the basement rocks and Paleoproterozoic to Mesoproterozoic sedimentary sequences (Wu et al., 2009; Zhang et al., 2007a). The Mesoarchean–Paleoproterozoic basement shows a wide range in ε_{Nd-Hf} composition, suggesting derivation from depleted mantle and enriched crust (Hu et al., 2000; Long et al., 2010). Less is known about Mesoproterozoic–Neoproterozoic history of the Tarim craton. However, recently discovered Proterozoic-age zircon grains both in metasedimentary and igneous rocks may indicate the existence of extensive Mesoproterozoic–Neoproterozoic basement in the Tarim craton (Cao et al., 2011; Ge et al., 2012; Long et al., 2011; Ma et al., 2012; Wang et al., 2009; Wu et al., 2009; Zhang et al., 2007a).

Phanerozoic sedimentation in the Tarim basin records an important transition from marine to continental facies during Late Carboniferous–Early Permian (Chen et al., 2006; and references therein, Fig. 1d). This transition in sedimentation facies was accompanied by massive intraplate mafic–ultramafic magmatism and felsic magmatism which is known as the Tarim LIP (Li et al., 2011, 2012; X. Yu et al., 2011; Yang et al., 2006b; Zhang et al., 2010; Zhou et al., 2009). A close link is suggested between felsic and mafic–ultramafic rocks (Tian et al., 2010; Zhang et al., 2010).

Drilling and log records reveal an extensive area (48,000 km^2) of felsic volcanic rocks in northern Tarim basin, which mainly consist of rhyolites, minor andesites and ignimbrites (Fig. 1d). The thickness of the felsic volcanic layer ranges from 100 to 300 m (Fig. 1d). Tian et al. (2010) recognized two different groups in the Tarim rhyolites: Group 1 rhyolites show an OIB-like affinity, whereas Group 2 rhyolites exhibit crustal signatures, which are consistent with a derivation by melting of pre-existing crustal basement. Zircon LA-ICPMS and SIMS U–Pb dating show a broad range of eruption ages from 291 to 272 Ma (ShangGuan et al., 2011; Tian et al., 2010). Samples studied in this paper were collected from an outcrop at Wenquan near Baicheng County and from drill holes HA1, HA2, NK1, YX1, YX2, YM16, MN1 and SX1 in the desert-covered Tarim basin (Fig. 1c). The Wenquan rhyolites are located ~300 km north of the main occurrence of Tarim rhyolites (Fig. 1b and c) and are the only Permian rock type in this area. All the rhyolitic samples are fine- to medium-grained and contain quartz (5–10%) and feldspar (10–20%) as phenocrysts with a groundmass composed of quartzofeldspathic minerals (70–85%) (Fig. 1d).

3. Analytical methods

3.1. Major and trace elements

Whole rock major oxide analyses were carried out using X-ray fluorescence spectrometry (XRF, Rigaku ZSX-100e) on fused glass disks at Guangzhou Institute of Geochemistry, Chinese Academy of Sciences (GIGCAS), following the analytical procedures described by Goto and Tatsumi (1996), and analytical uncertainties are mostly between 1 and 5% (Li et al., 2006). Trace element concentrations were determined by utilization of PerkinElmer Sciex ElAN 6000 ICP-MS, following the techniques described by Liu et al. (1996). The USGS and Chinese National standards AGV-2, BHVO-2, GSR-1, GSR-2, GSR-3 and W-2 were chosen for calibrating element concentrations of the analyzed samples. Analytical uncertainties of REE and other incompatible element analyses are generally better than 5% (Supplementary Table 1).

3.2. Whole rock Sr–Nd isotopes

Sr and Nd isotopic ratios were measured with a Micromass Isoprobe Multi-Collector ICPMS at GIGCAS. Sr and rare earth elements were first separated by cation exchange columns, followed by REE separation

Fig. 1. Simplified geological map of Tarim craton (a, modified after Jahn et al. (2000); b–c, modified after Tian et al. (2010) and XJBGMR (1993)) and lithological stratigraphical sections (d) of representative drilling holes recovered from the northern Tarim basin, showing significant transition from marine sedimentation to terrigenous–volcanogenic sedimentation during Late Carboniferous–Early Permian. Distribution area of felsic volcanics in (c) is based on drilling records and logs in (d). Numbers beside the lithology sections denote the drilling depth (d). Published zircon U–Pb dates of rhyolites (Tian et al., 2010) are marked in (d). The Northern margin of Tarim is also called South Tianshan Orogenic belt in other literature. Inset micrograph on the bottom showing extrusive texture of the high Nb–Ta rhyolites. Letters C, P and Cz beside lithology sections in (d) denote Carboniferous, Permian and Cenozoic respectively.

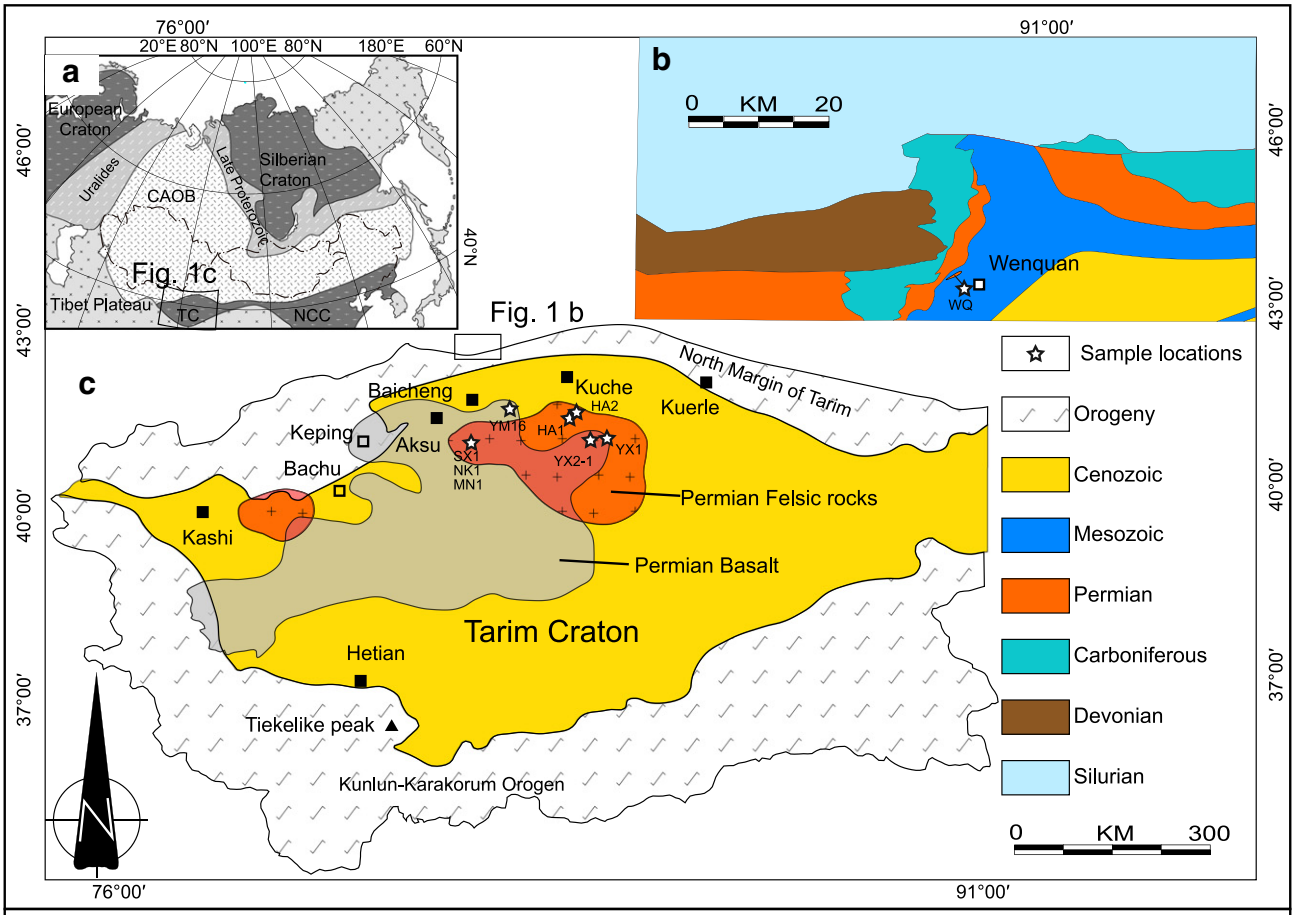
a
European Craton
Uralides
CAOB
Late Proterozoic
Silberian Craton
Tibet Plateau
TC
NCC
Fig. 1c
Fig. 1 b
b
0 KM 20
Wenquan
WQ
c
North Margin of Tarim
Baicheng
Kuche
Kuerle
HA2
YM16
HA1
Keping
Aksu
SX1
NK1
MN1
YX2-1
YX1
Bachu
Permian Felsic rocks
Kashi
Permian Basalt
Tarim Craton
Hetian
Tiekelike peak
Kunlun-Karakorum Orogen
Sample locations
Orogeny
Cenozoic
Mesozoic
Permian
Carboniferous
Devonian
Silurian
0 KM 300
76°00′
91°00′
46°00′
43°00′
40°00′
37°00′

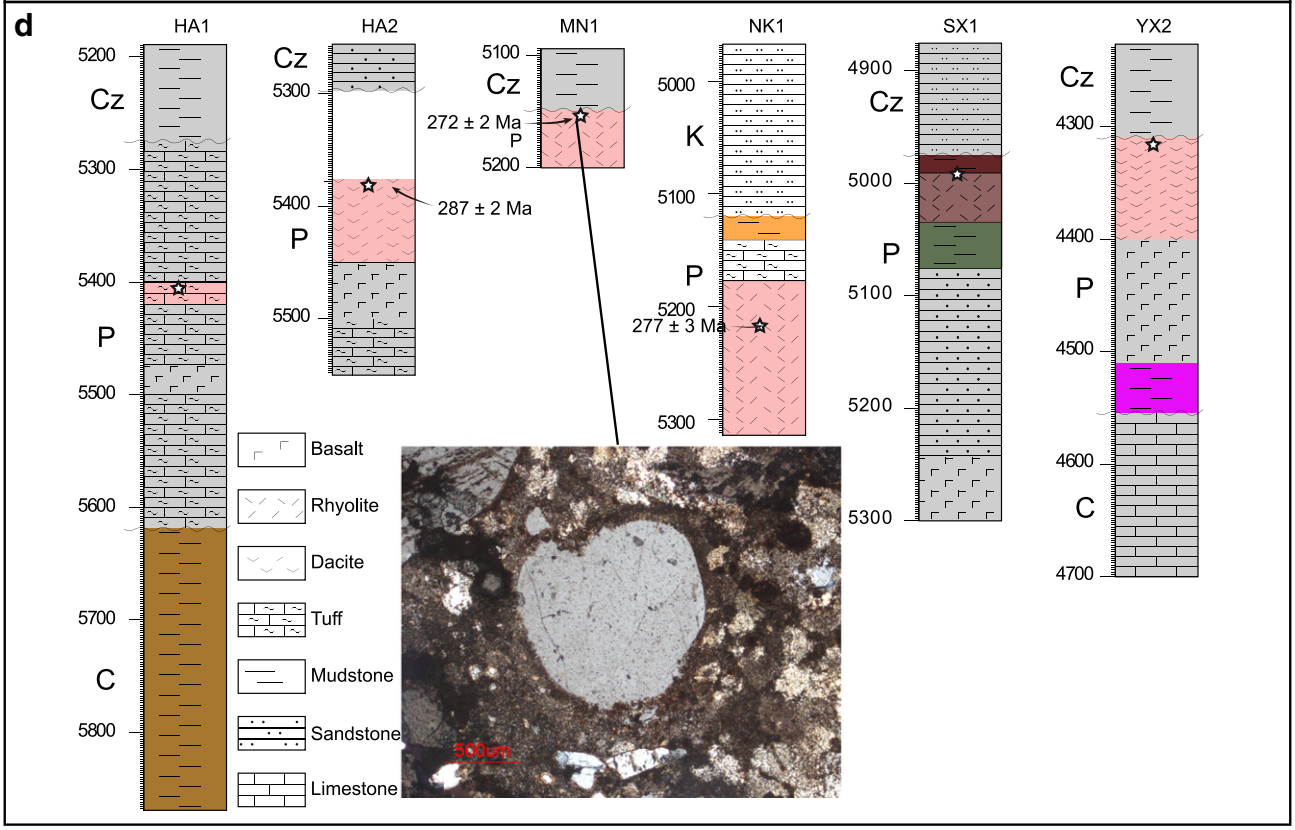
d
HA1
HA2
MN1
NK1
SX1
YX2
Cz
P
C
K
272 ± 2 Ma
287 ± 2 Ma
277 ± 3 Ma
Basalt
Rhyolite
Dacite
Tuff
Mudstone
Sandstone
Limestone
500μm

using HDEHP-coated Kef columns to obtain Nd. Detailed analytical procedures can be found in Wei et al. (2002) and Liang et al. (2003). BHVO-2 was used as the standard to monitor the instrumental performance for Sr and Nd isotopes. Multiple analyses of BHVO-2 yield an average of 0.703483 ± 6 (2σ) for $^{87}Sr/^{86}Sr$ ratio and an average of 0.512945 ± 9 (2σ) for $^{143}Nd/^{144}Nd$ ratio.

3.3. In situ zircon Hf–O isotopic analyses and zircon CA-TIMS U–Pb dating

Zircon grains from the sample WQ09 were separated into two fractions: One fraction for in situ O–Hf isotope analyses (WQ09-1) and the other fraction for zircon CA-TIMS U–Pb dating (WQ09-2). Pre-analytical cathodoluminescence (CL) imaging and in situ O–Hf isotopes were carried out at the Institute of Geology and Geophysics, Chinese Academy of Sciences in Beijing, China (IGGCAS).

Zircon oxygen isotopes were measured using Cameca IMS 1280. The Cs + primary ion beam was accelerated at 10 kV, with an intensity of ca. 2 nA and rastered over a 10 μm area. The spot is around 20 μm in diameter (10 μm beam diameter and 10 μm raster). The instrumental mass fractionation factor (IMF) was corrected using zircon standard Penglai ($\delta^{18}O$ = 5.3‰, Li et al., 2010) and Qinghu ($\delta^{18}O$ = 5.4‰, Li et al., 2013) for WQ09-1 and HA2, respectively. The internal precision of a single analysis was generally better than 0.2‰ for $^{18}O/^{16}O$. Measured $^{18}O/^{16}O$ is normalized by using VSMOW compositions, then corrected for the IMF. Detailed analytical procedures are provided by Li et al. (2010).

Zircon Lu–Hf isotopes were measured using multi-collector inductively coupled plasma mass spectrometry (MC-ICPMS) equipped with

Table 1
Major (wt %) and trace (ppm) elements for rhyolitic rocks from the Tarim Large Igneous Province.

Low Nb–Ta rhyolites										High Nb–Ta rhyolites		
Type	Rh	Rh	Rh	Rh	Rh	Da	Da	Da	Da	Da	Rh	Rh
Location	Wenquan			Tarim basin						Tarim basin		
Sample	wq09-1	wq09-2	wq09-3	HA1	NK1-3	HA2-1	HA2-2	YX1	YX2	SX1	MN1	YM16-2
SiO_2	71.16	71.57	68.35	71.79	76.72	66.34	65.78	68.15	67.09	63.77	74.62	78.60
TiO_2	0.57	0.54	0.60	0.47	0.36	0.63	0.60	0.63	0.70	0.91	0.21	0.22
Al_2O_3	13.81	13.80	14.50	14.06	11.92	14.96	14.67	14.04	13.91	16.59	12.55	10.20
Fe_2O_3T	4.20	3.85	5.27	2.46	0.94	4.88	5.33	4.50	5.43	5.55	1.66	2.48
MnO	0.05	0.04	0.07	0.04	0.00	0.10	0.12	0.08	0.09	0.04	0.01	0.01
MgO	0.33	0.36	0.38	0.11	0.13	0.41	0.37	0.42	0.56	0.41	0.22	0.16
CaO	0.74	0.26	0.34	1.15	0.38	2.25	2.46	2.17	2.19	0.94	0.74	0.07
Na_2O	2.75	3.43	2.82	3.46	1.89	3.83	3.51	3.07	2.91	4.70	0.63	0.68
K_2O	3.96	4.30	5.46	5.23	5.97	4.97	5.02	5.12	4.89	4.96	8.03	5.73
P_2O_5	0.11	0.06	0.08	0.13	0.08	0.19	0.18	0.19	0.21	0.27	0.01	0.01
L.O.I	1.84	1.28	1.62	0.58	1.12	0.92	1.45	1.13	1.52	1.35	0.80	1.32
Total	99.52	99.48	99.49	99.47	99.48	99.47	99.48	99.49	99.51	99.49	99.47	99.47
ICPMS (ppm)												
Sc	7.2	5.7	6.2	8.0	5.8	10.3	10.4	8.1	8.4	13.3	4.1	2.9
V	10.7	14.2	16.0	8.8	8.3	12.3	11.7	15.5	17.8	3.9	3.7	3.0
Cr	12.8	82.1	57.4	10.9	11.9	12.0	12.2	15.3	19.1	9.1	7.6	9.4
Mn	365.2	245.9	476.4	318.3	11.1	766.5	926.4	608.0	729.6	350.2	49.1	58.7
Co	55.2	2.7	3.3	117.3	33.2	3.3	3.6	3.9	5.0	17.0	132.4	64.8
Ni	7.1	9.6	10.5	7.4	6.1	7.2	7.0	8.1	8.7	5.5	7.1	6.2
Cu	7.3	6.7	6.9	35.8	4.4	9.2	8.6	10.7	10.5	6.5	4.3	2.3
Zn	117.9	90.9	101.2	90.2	17.8	128.8	116.3	93.0	104.9	99.9	66.8	120.1
Ga	34.8	22.8	26.3	34.3	25.3	36.9	38.2	29.5	30.0	61.8	25.3	14.4
Ge	1.2	1.8	1.9	1.1	1.1	1.3	1.3	1.2	1.3	1.3	1.1	1.1
Rb	118.3	103.1	139.8	157.5	184.1	134.6	139.9	213.1	199.0	95.5	161.7	514.2
Ba	1165	1922	1143	1140	808	1204	1257	865	918	4778	412	74
Sr	94.5	78.0	56.4	143.7	73.9	154.2	212.2	139.3	136.4	232.0	33.8	22.2
Y	42.5	36.0	51.8	30.1	42.7	52.5	52.7	53.5	47.8	29.5	56.9	85.0
Zr	543.4	433.1	428.7	457.7	432.8	632.8	590.6	466.8	517.7	451.3	646.6	1199.0
Nb	44.8	43.0	47.4	41.8	26.4	45.4	45.2	29.2	30.5	53.5	70.7	154.1
Cs	3.6	3.6	3.5	2.6	4.0	2.2	2.9	8.4	8.1	1.2	1.0	1.1
La	78.0	71.1	76.8	91.3	78.0	83.3	80.6	84.0	78.1	70.4	142.7	275.7
Ce	161.0	136.7	157.4	182.8	157.3	168.0	162.3	167.5	158.3	143.0	255.3	387.3
Pr	18.8	16.2	18.0	21.5	18.8	19.9	19.6	19.7	18.3	16.1	27.8	32.7
Nd	70.4	59.5	66.2	82.3	70.6	76.7	75.6	72.6	68.0	60.7	105.9	113.0
Sm	12.4	10.8	12.5	13.5	12.5	13.9	13.7	12.8	12.0	10.3	18.3	19.8
Eu	2.5	2.3	2.3	2.3	1.6	2.7	2.6	1.8	1.8	4.9	2.1	0.6
Gd	10.4	9.5	10.8	10.7	10.7	12.3	11.9	11.3	10.6	8.5	15.6	17.2
Tb	1.6	1.4	1.6	1.4	1.6	1.9	1.9	1.7	1.7	1.3	2.3	2.8
Dy	9.0	7.4	9.5	6.8	8.8	10.8	10.4	10.0	9.3	6.4	11.8	16.3
Ho	1.9	1.5	2.0	1.3	1.8	2.2	2.2	2.1	2.0	1.2	2.3	3.4
Er	4.8	4.1	5.4	3.4	4.8	5.8	5.6	5.5	5.1	3.1	6.1	8.8
Tm	0.7	0.6	0.8	0.5	0.7	0.8	0.8	0.8	0.8	0.4	0.9	1.3
Yb	4.6	4.1	5.1	3.0	4.9	5.6	5.4	5.2	5.1	2.6	5.6	8.2
Lu	0.7	0.6	0.8	0.5	0.7	0.9	0.8	0.8	0.8	0.4	0.8	1.2
Hf	13.3	11.1	10.4	11.3	10.2	14.7	14.1	11.6	12.4	10.1	15.1	31.5
Ta	2.9	2.6	2.7	2.9	1.8	2.7	2.7	2.1	2.1	3.6	5.1	10.5
Pb	15.2	27.7	10.9	21.9	23.8	22.8	23.9	35.4	32.4	13.5	8.2	21.9
Th	16.5	15.9	16.7	16.2	20.7	14.2	14.0	23.1	21.6	9.7	11.1	37.3
U	2.7	2.8	3.1	2.9	3.0	2.9	3.0	5.5	5.4	1.5	2.4	5.6
Tzr (°C)	936	904	900	886	901	896	887	872	885	878	940	–

Rh = Rhyolite, Da = Dacite. Tzr (°C) = Zircon saturation temperature.

a 193 nm laser at IGGCAS, following the analytical procedures described by Wu et al. (2006). Lu–Hf isotopic data were obtained on the same area in zircon grains where O isotopes were previously analyzed (WQ09-1 and HA2), with ablation spot size of ~44 μm in diameter and laser repetition rate of 6 Hz at 100 mJ. Using the same MC-ICPMS equipped with a 193 nm laser (RESOlution M-50-LR) and following similar procedures described by Wu et al. (2006), Hf isotopic data for sample MN1-2 was acquired at GIGCAS.

Zircon sample preparation and CA-TIMS U–Pb (Mattinson, 2005) analyses were carried out at the Berkeley Geochronology Center. By usage of techniques described in Mundil et al. (2004) and Mattinson (2005), zircon grains were pretreated (thermal annealing followed by chemical abrasion) to minimize the Pb loss. Detailed analytical procedures are given by Mundil et al. (2004). Comparison of the age results is facilitated by inter-laboratory cross calibration (Black et al., 2003, 2004) and analyses of reference materials (Mundil et al., 2004) as well as analyses of calibration solution distributed by the Earthtime initiative (Irmis et al., 2011). Zircon age was calculated using ISOPLOT 3.23 (Ludwig, 2003).

4. Results

4.1. Zircon U–Pb dating

Representative zircon CL images are shown in Supplementary Fig. 1. Zircon grains selected for isotopic analysis are transparent and colorless

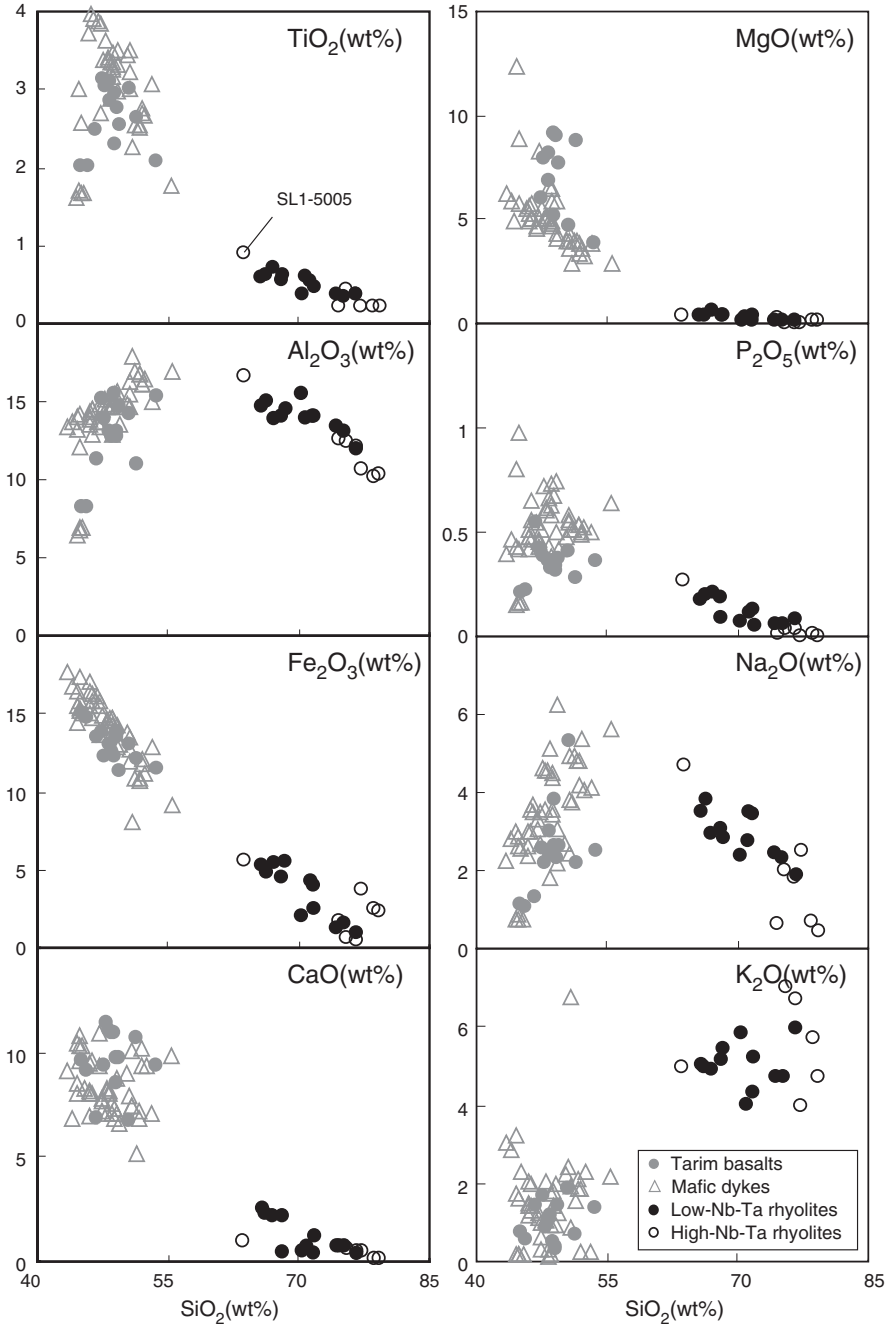

Fig. 2. Major oxides versus silica contents for the rhyolites from the Tarim LIP. Data for G1 rhyolites from Tian et al. (2010) are incorporated into the high Nb–Ta rhyolites whereas G2 rhyolites from Tian et al. (2010) are incorporated into the low Nb–Ta rhyolites classified in this study. Data of mafic magmas (Tian et al., 2010; Wei et al., 2014; Yang et al., 2007; Zhang et al., 2010; Zhou et al., 2009) are also shown for comparison.

in transmitted light, with lengths of 100 to 200 μm and width to length ratios of 1:1 to 1:2. Fine oscillatory zoning (Supplementary Fig. 1) and high Th/U ratios of 0.6–0.8 (Supplementary Table 2) of zircons indicate a magmatic origin.

Zircon CA-TIMS U–Pb isotopic data are given in Supplementary Table 2 and the concordia plot is presented in Supplementary Fig. 2. Twelve randomly picked zircon grains from sample WQ09-2 yield a coherent group with a weighted mean $^{206}Pb/^{238}U$ age of 286.8 ± 0.5 Ma (2σ; MSWD = 2.0, Supplementary Fig. 2). This age is similar to the SIMS age previously obtained for HA2 (287.3 ± 2.0 Ma, ShangGuan et al., 2011).

4.2. Whole rock geochemistry

Whole rock elemental analyses are listed in Table 1 along with published data from the Tarim rhyolites (Tian et al., 2010). Although both dacite and rhyolite are present in Tarim, the collective term "rhyolite" is used for simplicity. Samples with depletion in Nb and Ta are termed as low Nb–Ta rhyolites while samples with enrichment of Nb and Ta are termed as high Nb–Ta rhyolites. Within this classification scheme, samples from Wenquan and drilling holes HA1, HA2, NK1, YX1 and YX2, and G2 rhyolites in Tian et al. (2010) belong to the low Nb–Ta rhyolites, whereas samples from drill holes SX1, MN1 and YM16, and G1 rhyolites in Tian et al. (2010) belong to the high Nb–Ta rhyolites.

The data of mafic rocks (Tian et al., 2010; Wei and Xu, 2011; Yang et al., 2007; Zhang et al., 2010; Zhou et al., 2009) are also presented in Fig. 2 for comparison. A significant gap in SiO_2 content (Daly Gap) occurs between 56 wt.% and 64 wt.% (Fig. 2). Within the rhyolites, major oxides, with the exception of K_2O, are negatively correlated with SiO_2 (Fig. 2), indicative of crystal fractionation control by plagioclase, pyroxenes, apatite and Fe–Ti oxides. All but one high Nb–Ta rhyolites are more evolved than the low Nb–Ta rhyolites by showing higher SiO_2 and lower Al_2O_3, CaO, Fe_2O_3, MnO, Na_2O, P_2O_5 and TiO_2 contents. Sample SX1-5005 has the least-evolved geochemical composition. All the rhyolites have high A/CNK ratios (= molar $Al_2O_3/CaO + Na_2O + K_2O$) of 0.94 to 1.37 and A/NK ratios (= molar $Al_2O_3/Na_2O + K_2O$) of 1.24 to 1.57, indicating their metaluminous to peraluminous characteristics (Table 1 and Fig. 3a).

Data for silicic rocks from other LIPs (Etendeka and Emeishan) are also shown on Fig. 3. High Ga/Al ratios (>2.66), $Fe^{\#}$ (0.78–0.92), HFSEs (Zr and Nb), and zircon saturation temperatures (872–940 °C, M = 1.1–1.7; Table 1) mean that the Tarim rhyolites resemble A-type granitoids both from orogenic belt (Lachlan fold belt) and LIPs (Fig. 3b, c and d).

The low Nb–Ta and high Nb–Ta rhyolites from Tarim exhibit essentially similar trace element compositions, characterized by LREE-enrichment and negative anomalies in Ba, Sr, P, Eu and Ti (Fig. 4). An exception to this is sample SX1-5005, which shows positive Ba and Eu anomalies (Fig. 4d). The high Nb–Ta rhyolites are characterized by small negative to positive Nb–Ta anomalies, a feature resembling the coeval mafic dykes from Bachu (Fig. 4d). The low Nb–Ta rhyolites, however, exhibit significant negative Nb and Ta anomalies (Fig. 4c), which distinguish themselves from both the basaltic rocks and the high Nb–Ta rhyolites.

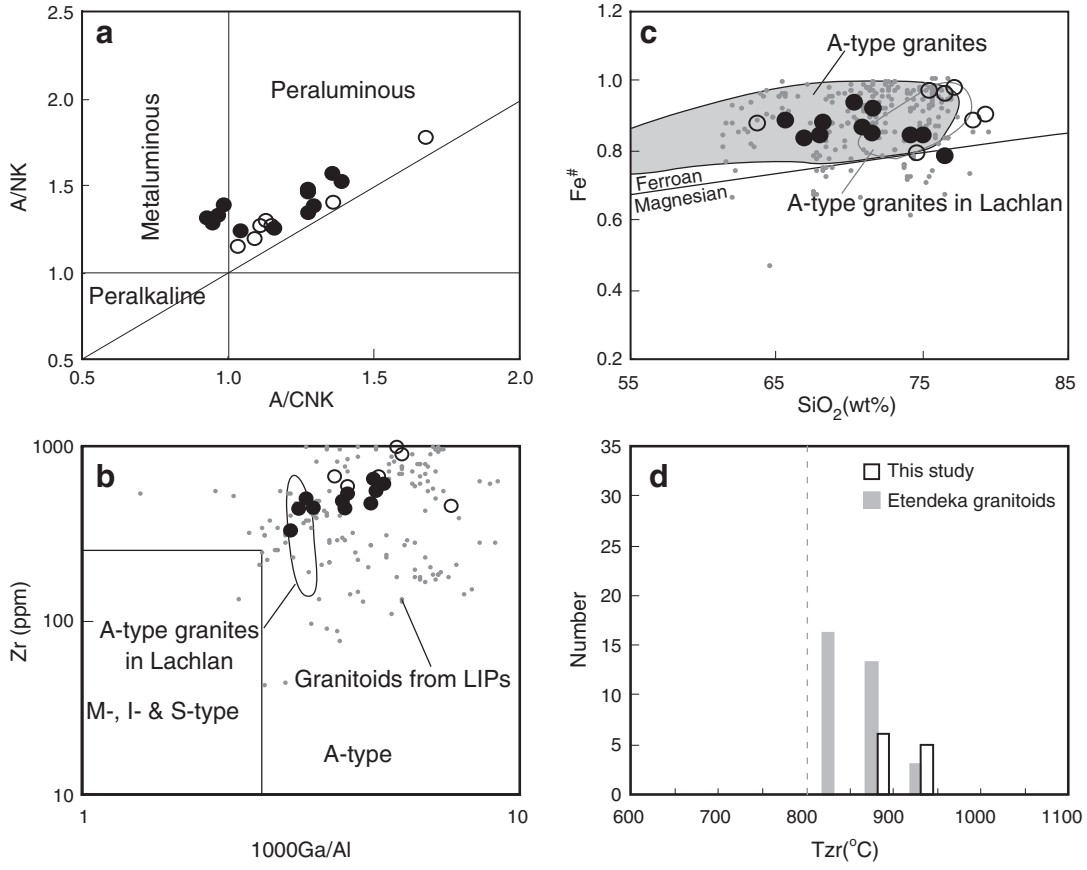

Fig. 3. Chemical classification diagrams for the Tarim rhyolites. (a) A/NK vs. A/CNK diagram showing that the low Nb–Ta and high Nb–Ta rhyolitic rocks are metaluminous to peraluminous. (b, c) Zr vs. Ga/Al and $Fe^{\#}$ and SiO_2 plot showing the characteristics of A-type granitoids for the low Nb–Ta and high Nb–Ta rhyolites from Tarim. (d) Comparison of zircon saturation temperature estimates between Tarim rhyolites and Etendeka granitoids. Data of granitoids from Lachlan Fold belt (Collins et al., 1982) and LIPs (Emeishan: Shellnutt and Jahn, 2010; Shellnutt and Zhou, 2007; Zhong et al., 2007, 2011; Xu et al., 2010; Etendeka: Ewart et al., 1998; Haapala et al., 2007; Frindt et al., 2004; Trumbull et al., 2004; Mingram et al., 2000; Schmitt et al., 2000; Harris et al., 1999) were also presented for comparison.

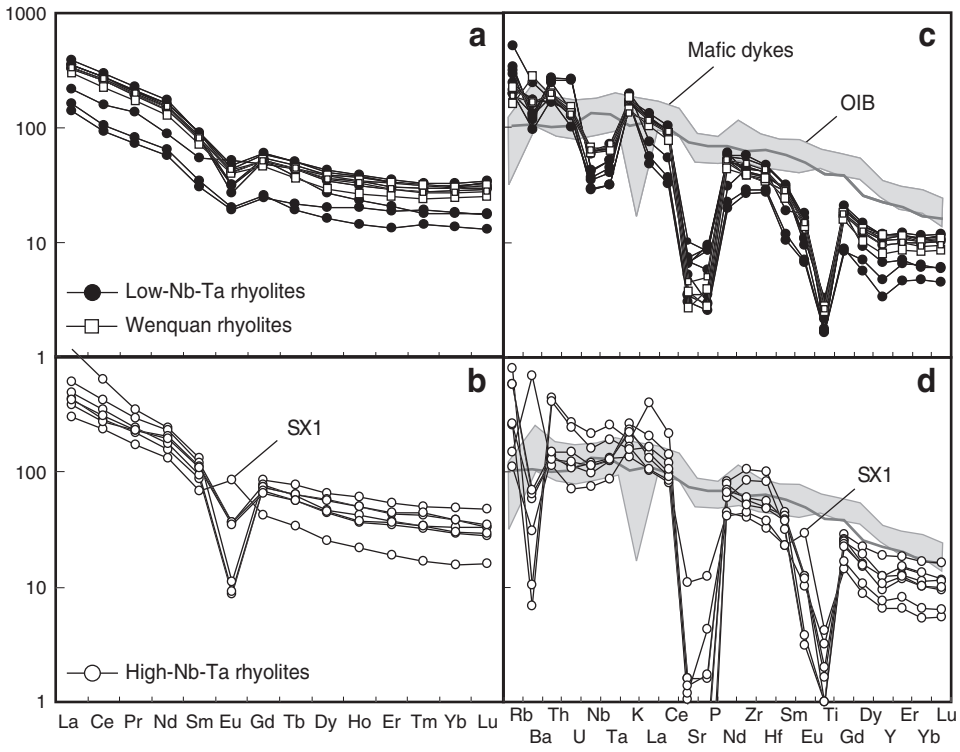

Fig. 4. Chondrite-normalized rare earth element patterns (left panel) and primitive mantle-normalized multi-element diagram (right panel) of Tarim rhyolites and mafic dykes. Data source for mafic dykes are the same as in the caption of Fig. 2. OIB and normalizing values are from Sun and McDonough (1989).

Zirconium is used as a differentiation index in the plots of trace element variation diagrams (Fig. 5), as it behaves incompatibly throughout the magmatic sequence and is stable during post-eruption processes. In the plots of Nb, Th and U against Zr, and Nb/La against Th/La, the high Nb–Ta rhyolites and the mafic magmas from Tarim have similar trace element ratios (Fig. 5a, b, c and d), suggesting that they may have shared a similar source. In contrast, the low Nb–Ta rhyolites deviate significantly from the trend of high Nb–Ta rhyolites (Fig. 5), suggesting a different source. In the plot of Sr and Eu against Zr, the low Nb–Ta and high Nb–Ta rhyolites define different trends from the mafic rocks (Fig. 5e, f).

4.3. Sr–Nd isotopes

The measured whole rock Sr and Nd isotopic ratios and calculated initial ratios are shown in Table 2. The low Nb–Ta rhyolites have low $\varepsilon_{Nd}(t)$ values of −7.7 to −5.6, with initial $^{87}Sr/^{86}Sr$ ratios of 0.7067 to 0.7109. Their single stage Nd model ages (T_{DM}) range from 1355 to 1542 Ma. Compared to the low Nb–Ta rhyolites, the high Nb–Ta rhyolites exhibit higher $\varepsilon_{Nd}(t = 287\ Ma)$ values of −3.4 to +1.3, corresponding to T_{DM} of 864 to 1211 Ma, and lower initial $^{87}Sr/^{86}Sr$ ratios of 0.7055 to 0.7072 (Table 2 and Fig. 6). The wide range of initial $^{87}Sr/^{86}Sr$ ratios is likely due to error propagation from variable $^{87}Rb/^{86}Sr$ ratios (Jahn et al., 2000), thus limiting the use of $^{87}Sr/^{86}Sr$ in petrogenetic discussion. Nevertheless, their ε_{Nd} values overlap with the associated basaltic rocks in Tarim (Fig. 6). Most of low Nb–Ta rhyolites lie within the field of Tarim basement (Fig. 6). Three samples are isotopically intermediate between Tarim basalts and Tarim basement (Fig. 6).

4.4. Zircon Hf–O isotopes

Zircons from the rhyolite (WQ09-1) and dacite (HA2) show similar $^{176}Hf/^{177}Hf$ values that range from 0.282452 to 0.282575 (Supplementary Table 3). Their initial $\varepsilon_{Hf}(t = 287\ Ma)$ values are −4.4 to −1.1 for WQ09-1 and −5.2 to −0.8 for HA2, respectively (Supplementary Table 3 and Fig. 7). Calculated zircon Hf model ages (T_{DM2}) are between 1.35 and 1.63 Ga. Thirty-two analyses for MN1-2 yield $^{176}Hf/^{177}Hf$ values from 0.282626 to 0.282850, with initial ε_{Hf} range of 0.7 to 8.2 (Supplementary Table 3 and Fig. 7a) and T_{DM2} range of 0.77 and 1.25. Thirty spot analyses of oxygen isotopes were performed on samples WQ09-1 and HA2 respectively. $\delta^{18}O$ values of zircons from WQ09-1 range from 8.1 to 9.6‰, and are essentially identical to those of HA2 (7.7 to 9.2‰, Supplementary Table 3 and Fig. 7b).

5. Discussion

5.1. Emplacement age of the Tarim rhyolites and their relationship with mafic rocks

The U–Pb age of 286.8 ± 0.5 Ma obtained by CA-TIMS analyses for the sample WQ09 is within the age range previously determined for the rhyolites (291–272 Ma) from the northern Tarim basin (Tian et al., 2010; and Fig. 1d). Fig. 8 summarizes available emplacement ages of the Tarim rhyolites. In order to gain insights into their relationship with mafic magmatism, recent compiled chronological data of mafic rocks are shown together in Fig. 8.

Fig. 8 shows two major episodes of mafic–ultramafic magmatism in the Tarim LIP (Chen et al., 2010; Wei et al., 2014; Xu et al., 2013): the first episode of magmatism has a time span from 291 to 287 Ma and is represented by major flood basalts; the second episode of magmatism (283–272 Ma) is represented by mafic–ultramafic intrusions/dykes. Most of the low Nb–Ta in this study and all the high Nb–Ta rhyolites correspond to the first and second periods of mafic magmatism, respectively (Fig. 8). The earlier emplacement of the low Nb–Ta rhyolites is consistent with their close association with basalts in drill holes (Tian et al., 2010). Nevertheless, it should be noted that a few low Nb–Ta rhyolites (NK1-2 and NK1-3) in this study have zircon U–Pb ages of 277.3 ± 2.5 Ma (Tian et al., 2010), well within the range defined by the high Nb–Ta samples (283–272 Ma).

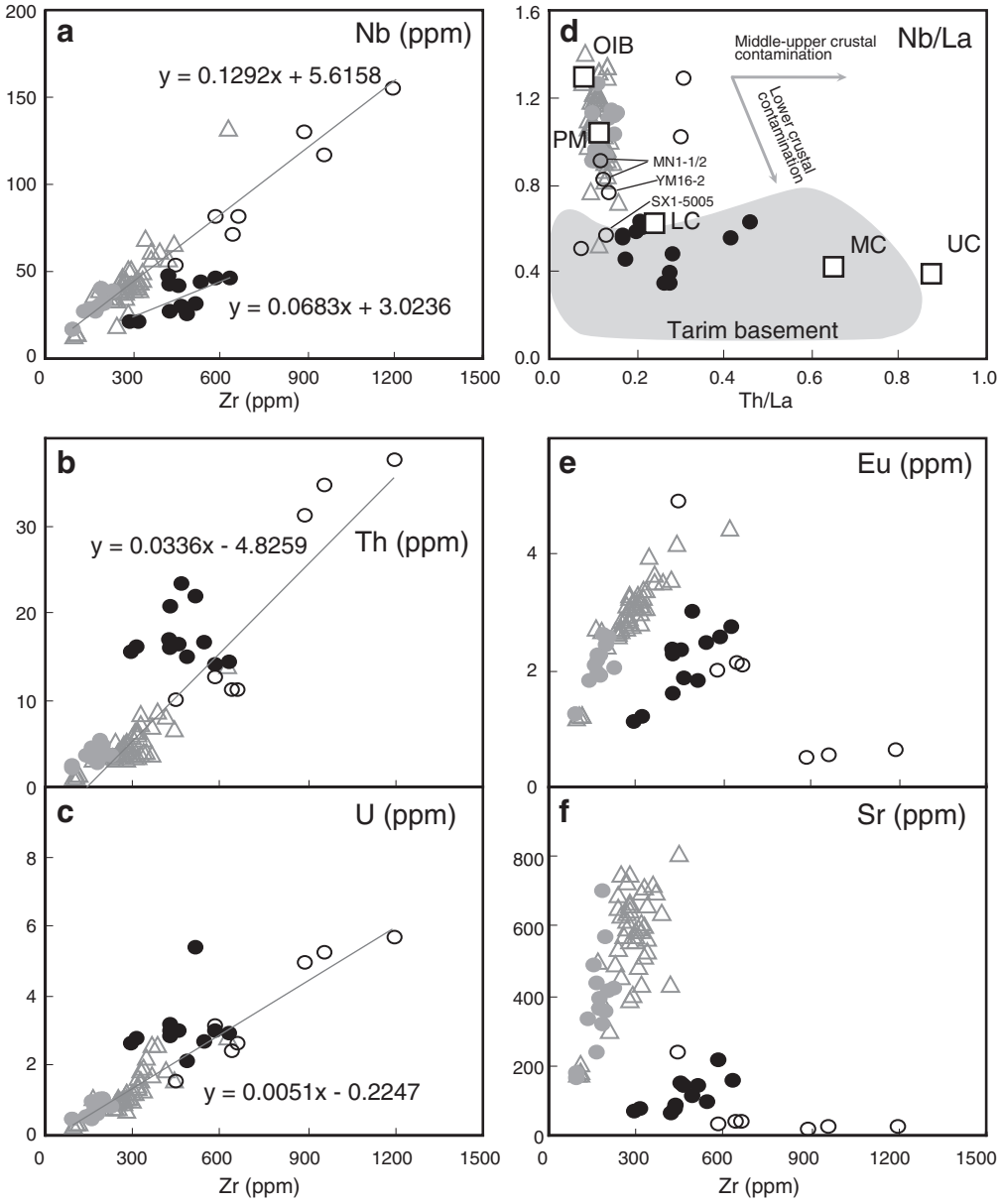

Fig. 5. Co-variation of selected trace elements and ratios for the Tarim rhyolites and mafic magmas. Data source for mafic magmas are the same as in the caption of Fig. 2. The data of the Tarim basement in (d) are from Cao et al. (2011), Chen et al. (2000), Hu et al. (2000), Jiang et al. (2005), and Zhang et al. (2007b, 2009, and 2012). Data of OIB and PM are from Sun and McDonough (1989); Data of lower crust (LC), middle crust (MC) and upper crust (UC) are from Rudnick and Gao (2003).

Table 2
Whole rock Sr and Nd isotopic compositions for rhyolitic rocks from the Tarim Large Igneous Province.

	Rb (ppm)	Sr (ppm)	$^{87}Rb/^{86}Sr$	$^{87}Sr/^{86}Sr$	2σ	$^{87}Sr/^{86}Sr(i)$	Sm (ppm)	Nd (ppm)	$^{147}Sm/^{144}Nd$	$^{143}Nd/^{144}Nd$	2σ	$^{143}Nd/^{144}Nd(t)(i)$	$\varepsilon_{Nd}(t)$	T_{DM}(Ma)	$f_{Sm/Nd}$
Low Nb–Ta rhyolites															
WQ09-1	118.30	94.46	3.50	0.725157	6	0.710877	12.45	66.21	0.113668	0.512197	9	0.511983	−5.6	1457	−0.42
WQ09-2	103.10	78.04	3.69	0.721763	6	0.706699	10.81	59.54	0.109751	0.512169	7	0.511963	−6.0	1444	−0.44
HA1	157.50	143.70	3.06	0.721685	5	0.709188	13.53	82.32	0.099353	0.512137	6	0.511950	−6.2	1355	−0.49
NK1-3	184.10	73.89	6.96	0.737707	6	0.709298	12.47	70.63	0.106726	0.512179	8	0.511978	−5.7	1389	−0.46
HA2-2	139.90	212.20	1.84	0.718876	5	0.711359	13.74	75.60	0.109864	0.512149	8	0.511943	−6.4	1475	−0.44
YX1	213.10	139.30	4.27	0.727939	5	0.710496	12.83	72.59	0.106839	0.512073	9	0.511872	−7.7	1542	−0.46
YX2	199.00	136.40	4.07	0.727269	5	0.710634	11.98	67.98	0.106527	0.512100	9	0.511900	−7.2	1499	−0.46
High Nb–Ta rhyolites															
SX1	95.54	232.00	1.15	0.710217	6	0.705521	10.30	60.68	0.102614	0.512389	6	0.512196	−1.4	1048	−0.48
MN1[a]	365.51	34.02	11.81	0.755412	8	0.707184	18.26	105.90	0.104240	0.512532	8	0.512336	1.3	864	−0.47
YM16-2							19.75	113.00	0.105656	0.512295	7	0.512097	−3.4	1211	−0.46

[a] Rb and Sr abundances are from Tian et al. (2010). The initial isotopic ratios are calculated at 287 Ma.

5.2. Petrogenesis

5.2.1. Rock affinities

The data presented in this paper, together with those published in literature suggest that the rhyolites in the Tarim LIP are metaluminous to peraluminous with high Fe# number, Ga/Al ratios, Zr, Nb and REE contents and high zircon saturation temperatures (Fig. 3 and Table 1). These geochemical characteristics resemble A-type granitoids both in orogenic belts and LIPs (Fig. 3) (King et al., 1997). Furthermore, when combined with lithology and geochemistry, zircon saturation temperature estimates of granitoids could be a powerful tool for tectonic discrimination (Liu et al., 2013). Granitoids from subduction/collision-related settings have lower zircon saturation temperature estimates (generally < 800 °C) than those from plume-related settings (generally > 800 °C). Rhyolites in this study have high zircon saturation temperature estimates of 872–940 °C (Table 1 and Fig. 3d), resembling those of plume-related granitoids.

Combined with isotopic data, the aluminium saturation index and A/NK are good geochemical discriminators between granitoids of crustal and mantle origin (Barbarin, 1999), i.e., metaluminous and peraluminous granitoids reflect incorporation of a crustal component whereas peralkaline granitoids are of mantle origin. The Tarim rhyolites have ε_{Nd} values of −7.7 to +1.3. In the A/CNK vs. A/NK diagram (Fig. 3a), they straddle in the metaluminous to peraluminous fields, implying various extents of incorporation of crustal material. However, contrasting geochemical and isotopic compositions between the low Nb–Ta and high Nb–Ta rhyolites may imply different petrogenetic processes.

Extensive fractionation might have taken place during the formation of the Tarim felsic volcanics. Negative anomalies of Ba, Sr and Eu, and different trends in plot of Sr and Eu against Zr are suggestive of fractionation of feldspar. Negative P and Ti anomalies result from separation of apatite and Ti-bearing oxides, respectively. However, sample SX1-5005 exhibits positive Ba and Sr anomalies, consistent with accumulation of feldspar in this sample. Consequently, the trace element ratios, which are insensitive to fractionation, will be used in petrogenetic evaluation.

5.2.2. Low Nb–Ta rhyolites

Extreme fractionation of basaltic magma could produce A-type granitic magma (Turner et al., 1992). However, granitic magmas derived from primitive basaltic rocks are expected to contain magmatic zircons with mantle-like $\delta^{18}O$ values (~5.3 ± 0.3‰) (Valley et al., 2005). The Wenquan and HA2 rhyolites have $\delta^{18}O_{zircon}$ values of 7.7 to 9.6‰, consistent with a derivation from continental crustal source (Valley et al., 2005). Furthermore, the low Nb–Ta rhyolites from Tarim have negative anomalies of HFSEs (Nb, Ta and Ti) and positive anomalies of LILEs (large ion lithophile elements) on primitive mantle-normalized multi-element plots (Fig. 4) and have high initial $^{87}Sr/^{86}Sr$ ratios and

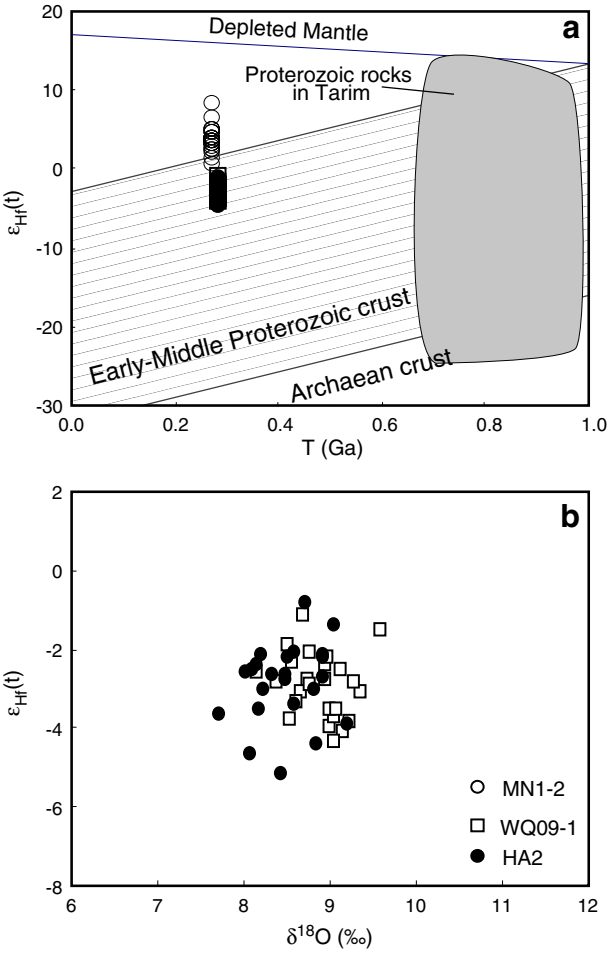

Fig. 7. Plots of initial $\varepsilon_{Hf}(t)$ vs. time and $\delta^{18}O$ (‰) for the Tarim rhyolites. (a) $\varepsilon_{Hf}(t)$ vs. time; (b) $\varepsilon_{Hf}(t)$ vs. $\delta^{18}O$ (‰). Field of Proterozoic rocks is from Wang et al. (2009), Ge et al. (2012), Ma et al. (2012) and Long et al. (2011).

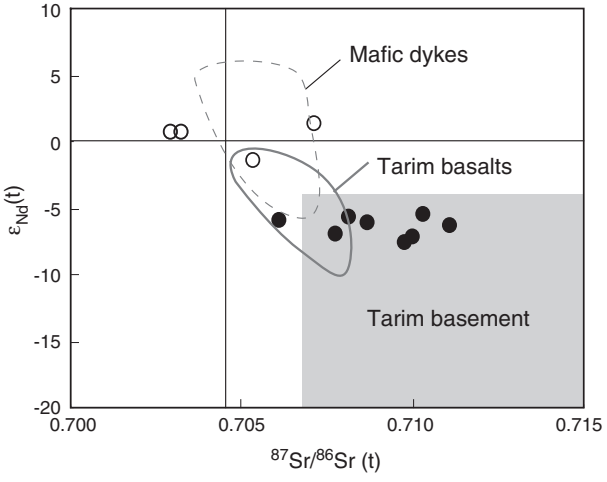

Fig. 6. Plot of initial $\varepsilon_{Nd}(t = 287\ Ma)$ and $^{87}Sr/^{86}Sr$ (t = 287 Ma) for the Tarim rhyolites and mafic magmas. Data source of mafic magmas are the same as in Fig. 2. The data of the Tarim basement are the same as in the caption of Fig. 5.

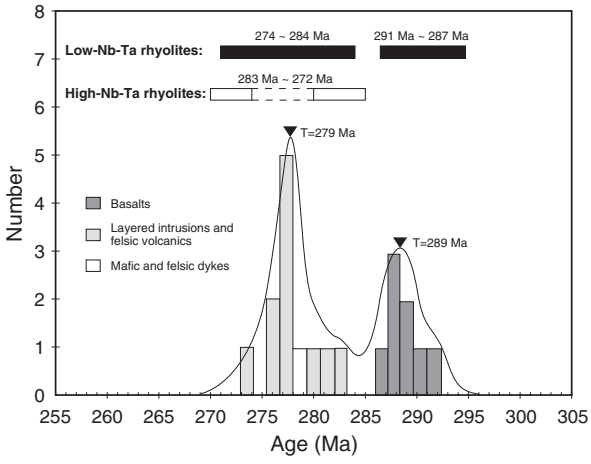

Fig. 8. Duration of low Nb–Ta and high Nb–Ta rhyolites in the Tarim Large Igneous Province. Age histogram and ages at peaks of probability curves are after Wei et al. (2014). Note that the low Nb–Ta rhyolites have two episodes of eruption age of 291–274 Ma and the high Nb–Ta rhyolites have age of 283–272 Ma. Data source for the low Nb–Ta and high Nb–Ta rhyolites are from Tian et al. (2010) and J.C. Yu et al. (2011).

negative $\varepsilon_{Nd}(t)$ and $\varepsilon_{Hf}(t)$ values (Figs. 6 and 7), indicative of significant involvement of continental crustal components in magma genesis (Rudnick and Gao, 2003).

Potential crustal source rocks responsible for production of aluminous A-type granitoids include granulites, tonalitic–granodioritic gneisses and metasedimentary rocks (Collins et al., 1982; Creaser et al., 1991; Huang et al., 2011; Skjerlie and Johnston, 1993). A granulitic residual source that had previously generated an I-type granite (Collins et al., 1982) is not favored because there is no evidence of such a granite type in Tarim. Derivation from a metasedimentary protolith model (Huang et al., 2011) is also excluded because the low Nb–Ta rhyolites have coupled Nd–Hf isotopes which are suggestive of partial melting of tonalitic–granodioritic protoliths (Creaser et al., 1991; Skjerlie and Johnston, 1993). This is supported by zircon Hf–O isotopes of the Wenquan and HA2 rhyolites (Fig. 7). Specifically, Hf isotopic model ages are consistent with a derivation from a protolith of Early–Middle Proterozoic crust (Wang et al., 2009). In fact, Proterozoic tonalites and granodiorites are present in the studied area (Long et al., 2011; Wu et al., 2009). This petrogenetic model is further supported by a plot of Th/La against Nb/La (Fig. 5d), in which most of the low Nb–Ta rhyolites plot within the field of the Tarim basement/continental crust (Cao et al., 2011; Chen et al., 2000; Hu et al., 2000; Jiang et al., 2005; Rudnick and Gao, 2003; Zhang et al., 2007b, 2009, 2012). Nevertheless, it should be pointed out that other low Nb–Ta rhyolites define a geochemical trend towards the middle–upper crust (Fig. 7d), probably due to crustal contamination.

The low Nb–Ta rhyolites have Sr–Nd isotopic composition that slightly overlaps with the associated basalts (Fig. 6). Although this suggests that the associated basalts may have been involved in the generation of the low Nb–Ta rhyolites, there is no mixing trend between the rhyolites and the basalt in Hf–O isotope space (Fig. 7b). Moreover, zircons from the low Nb–Ta rhyolites have $\delta^{18}O$ values identical to those of Tarim Precambrian crystalline basement (unpublished data), further arguing against significant involvement of basalts in the generation of the low Nb–Ta rhyolites.

5.2.3. High Nb–Ta rhyolites

Given the different compositional trends and trace element ratios (Fig. 5), the high Nb–Ta rhyolites are likely to have been generated by a different petrogenetic mechanism from the low Nb–Ta rhyolites. Ce/Yb ratios of the low Nb–Ta rhyolites increase with increasing Ce contents (Fig. 9a), a trend that can be best interpreted as variable degrees of partial melting (Allègre and Minster, 1978). In contrast, most high Nb–Ta rhyolites have nearly constant Ce/Yb ratios over a wide range of Ce contents (Fig. 9a). This trend highlights the role of crystal fractionation in the generation of the high Nb–Ta rhyolites. The least contaminated high Nb–Ta samples (MN1-1 and MN1-2, Figs. 5, 6, and 7) have a Sr–Nd–Hf isotopic composition and trace element ratios similar to associated mafic magmas in Tarim (Tian et al., 2010; Zhang et al., 2010). All these lend support to the suggestion that they are derived from the associated mafic magmas by crystal fractionation. The negative correlations between $\varepsilon_{Nd}(t)$ values and SiO_2 contents suggest that fractionation was associated with crustal contamination (Fig. 9b). The degree of crustal contamination is the highest for the samples YM16-2 and SX1-5005 because these samples have Nb/La and Th/La ratios straddling between the field between mafic magmas and the Tarim basement (Fig. 5d). This is further supported by the large variation of $\varepsilon_{Hf}(t)$ (8.2–0.7, Supplementary Table 3 and Fig. 7a) in zircon for MN1-2, which is best interpreted as a result of assimilation of ancient crust to mafic magmas. Specifically, the highest $\varepsilon_{Hf}(t)$ values represent the least contaminated mafic end-member, whereas the lowest $\varepsilon_{Hf}(t)$ values represent the most contaminated felsic end-member.

The high Nb–Ta rhyolites have trace element ratios that are indistinguishable from the basalts (Fig. 5), suggesting that the high Nb–Ta rhyolites might have been derived from the Tarim basalts. However, this is at odds with the contrasting isotopic composition between the two magma series; the Tarim basalts have negative ε_{Nd} and ε_{Hf} values which are interpreted as a derivation from an enriched lithospheric mantle (Li et al., 2012; Wei et al., 2014; Xu et al., 2013), whereas the least-contaminated high Nb–Ta rhyolites have positive ε_{Nd} and ε_{Hf}

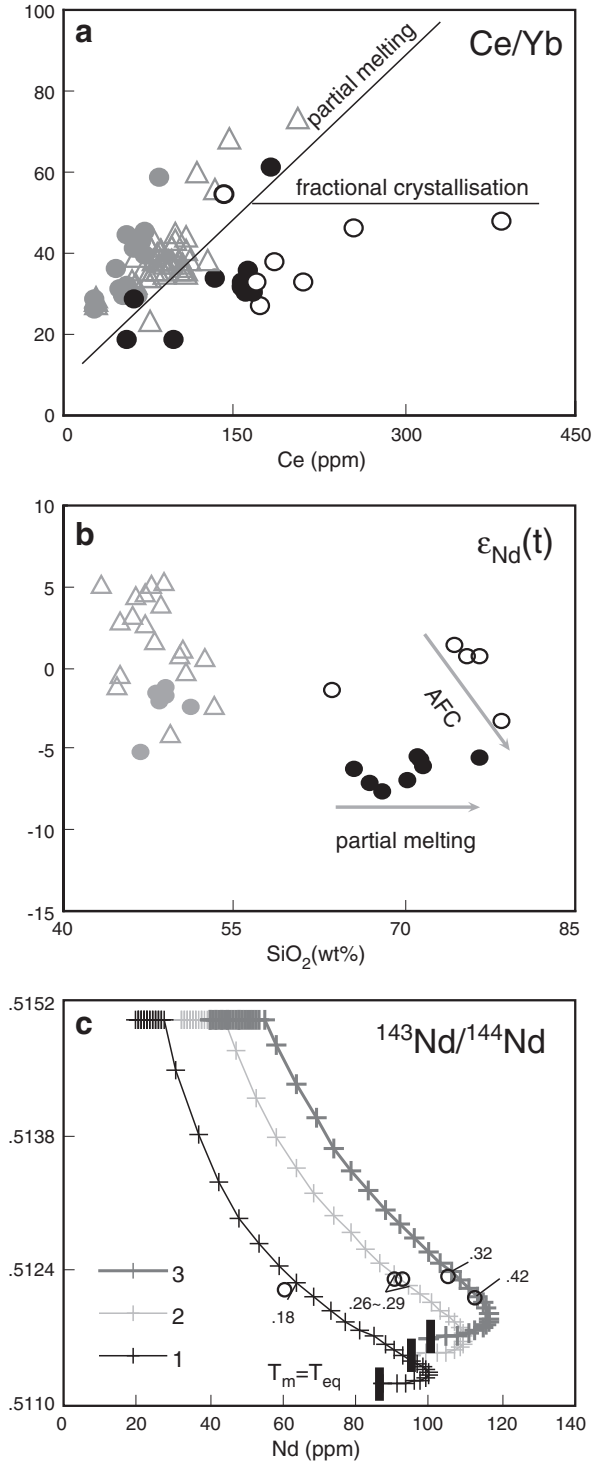

Fig. 9. Geochemical plots of major, trace elements and isotopes showing that the low Nb–Ta and high Nb–Ta rhyolites have different trends. (a) Ce/Yb vs. Ce; (b) Nb/La vs. Th/La; (c) $^{143}Nd/^{144}Nd(t)$ vs. Nd contents. The assimilation–fractionation crystallization process (c) is modeled using the EC-AFC method of Bohrson and Spera (2001) and Spera and Bohrson (2001). Numbers denote proportions of crustal materials involved in basaltic magma (normalized to original mass of magma body). Detailed information for the modeling can be found in the text and in Table 3.

Table 3
EC-AFC parameters for G2 rhyolites from the Tarim Large Igneous Province.

Thermal parameters	T(°C)		
Magma liquidus temperature	1300	Crystallization enthalpy	396000 J/kg
Magma initial temperature	1300	Fusion enthalpy	354000 J/kg
Assimilant liquidus temperature	850	Isobaric specific heat of magma	1484 J/kg K
Assimilant initial temperature	500	Isobaric specific heat of assimilant	1388 J/kg K
Solidus temperature	800		
Equilibration temperature	900		
Compositional parameters	**Source 1**	**Source 2**	**Source 3**
Magma initial concentration (ppm)	20	32	40
Magma isotope ratio	0.5150	0.5150	0.5150
Magma trace element partition coefficient	0.3	0.3	0.3
Assimilant initial concentration (ppm)	100	100	100
Assimilant trace element partition coefficient	0.5	0.5	0.5
Assimilant isotope ratio	0.5106	0.5106	0.5106
Total mass of melted wall-rock (normalized to original mass of magma body)	0.18	0.26–0.29	0.32–0.42

Computations were followed by utilization of computer program EC-AFC as cited in Bohrson and Spera (2001).

values, pointing to a mantle source. In addition, the Tarim basalts were emplaced 10 Ma earlier than the high Nb–Ta rhyolites and therefore, the high Nb–Ta rhyolites cannot be the fractionation products of the Tarim basalts. In the Tarim LIP, some intrusive plutons (e.g., Xiaohaizi syenite) are geochemically equivalent to the high Nb–Ta rhyolites. These plutons are essentially coeval with the mafic dykes in the northwestern Tarim basin and the high Nb–Ta rhyolites studied in this paper (~280 Ma). It is thus reasonable to assume basalts, similar in composition to the Tarim mafic dykes, were the parental magmas of the high Nb–Ta rhyolites.

The Energy-Constrained AFC model (EC-AFC) (Bohrson and Spera, 2001; Spera and Bohrson, 2001) was used to examine thermal, isotopic and chemical relationships between the mafic dykes and the rhyolites. In the modeling, 1300 °C, calculated from major element compositions of the Bachu mafic dyke (Zhou et al., 2009), was taken as magma liquidus temperature, the average zircon saturation temperature (Table 1) of ~900 °C, obtained from thermometric calculation, was taken as equilibrium temperature, and other thermal parameters were from Bohrson and Spera (2001). The assimilant component was compositionally similar to Tarim Precambrian basement rocks (Hu et al., 2000). Three different Nd abundances were used in the modeling because the high Nb–Ta rhyolites have variably high Nd abundances. Detailed parameters are listed in Table 3 and modeling results are presented in Fig. 9c. This shows that the compositional variation of the high Nb–Ta rhyolites can be accounted for by EC-AFC processes, with involvement ratios of Precambrian crustal materials ranging from 0.18 to 0.42 (total mass of melted wallrocks normalized to original mass of magma body) (Fig. 9c).

5.3. Implications for crustal melting above a mantle plume

Crustal melting triggered by a mantle plume can be subdivided into two types: conductive heating from underlying mantle and advective heating from basaltic magma that underplated at the crust–mantle boundary (Xu et al., 2008). The latter is more efficient than the former in inducing crustal partial melting. Crustal melting that is simultaneous with the flood basalt volcanism can only be accounted for by the advective heating transferred by underplated magma (Frost et al., 2001). When the plume head impacts on the base of thick lithosphere, it first induces partial melting of enriched components in lithospheric mantle, part of this basaltic magma may have ponded near the crust–mantle boundary due to the density contrast (Sparks et al., 1980). When basaltic magmas are emplaced into crustal levels, melting and generation of silicic magma can be expected (Annen and Sparks, 2002; Annen et al., 2006; Huppert and Sparks, 1988). The temperature of continental crust may reach in excess of 800 °C during continuous basalt injection, which is hot enough to induce partial melts (Annen and Sparks, 2002; Shellnutt et al., 2012). The low Nb–Ta rhyolites yield zircon saturation temperature estimates of 872–936 °C (Watson and Harrison, 1983). The temperature estimates are similar to the modeled temperatures of partial melting of the crust due to basalt injection (Annen and Sparks, 2002; Huppert and Sparks, 1988). Stratigraphic sections (Fig. 1d) and geochronological results (Supplementary Fig. 2 and Fig. 8) have shown that the low Nb–Ta rhyolites and basalts in the Tarim LIP are contemporaneous, which is also consistent with the modeling that partial melting of pre-existing crustal rocks would occur with negligible delay after arrival of the invading basalt ($<10^3$ years) (Annen and Sparks, 2002; Huppert and Sparks, 1988). An analogous example of crustal melting induced by under-plating basaltic magma can be found in the Snake River Plain-Yellowstone volcanic field (SRP-Y, USA), eruption of basalt induced by partial melting of the Yellowstone mantle plume was contemporaneous with emplacement of voluminous felsic magma derived from remelting of overlying crust (Coble and Mahood, 2012; Nash et al., 2006). In the Tarim case, most low Nb–Ta rhyolites of this study erupted simultaneously with the flood basalts. However, their geochemical compositions rule out a direct genetic linkage to the flood basalts. It is more likely that the basaltic magmas underplated at depths may have provided heat source for crustal melting to generate the low Nb–Ta rhyolites (Fig. 10a). As argued by X. Yu et al. (2011) and Wei et al. (2014), the ~290 Ma flood basalt volcanism was derived from the enriched lithospheric mantle as a result of conductive heating from an incubating plume. In this scenario, magma generation rate is relatively low, hampering the formation of large magma chambers. This explains the general absence of mafic–ultramafic complexes and high Nb–Ta rhyolites in the first magmatic stage in the Tarim LIP (Fig. 10a).

At ~280 Ma, the plume materials start to melt as a result of decompression, either due to lithospheric thinning or plume deflection (Wei et al., 2014). Relatively high magma generation rates ensure the development of magma chambers and plumbing systems at variable crustal levels. The effects of these magmatic fractionation systems on crust are two-folds: (a) Heat transfer from magmatic fractionation to surrounding crustal wall-rocks would involve crustal material in the course of crystal fractionation of mafic magmas, leading to the formation of the high Nb–Ta rhyolites; (b) Emplacement of magmas at variable crustal levels would also advectively heat up the crust, and eventually trigger crustal melting to produce the low Nb–Ta rhyolites. This geodynamic process accounts for the temporal and spatial association between high Nb–Ta rhyolites (and their plutonic equivalents such as syenites) and mafic–ultramafic complexes (Fig. 10b). It also explains why the low Nb–Ta rhyolitic magmatism lasted longer than the high Nb–Ta rhyolitic magmatism (Fig. 8).

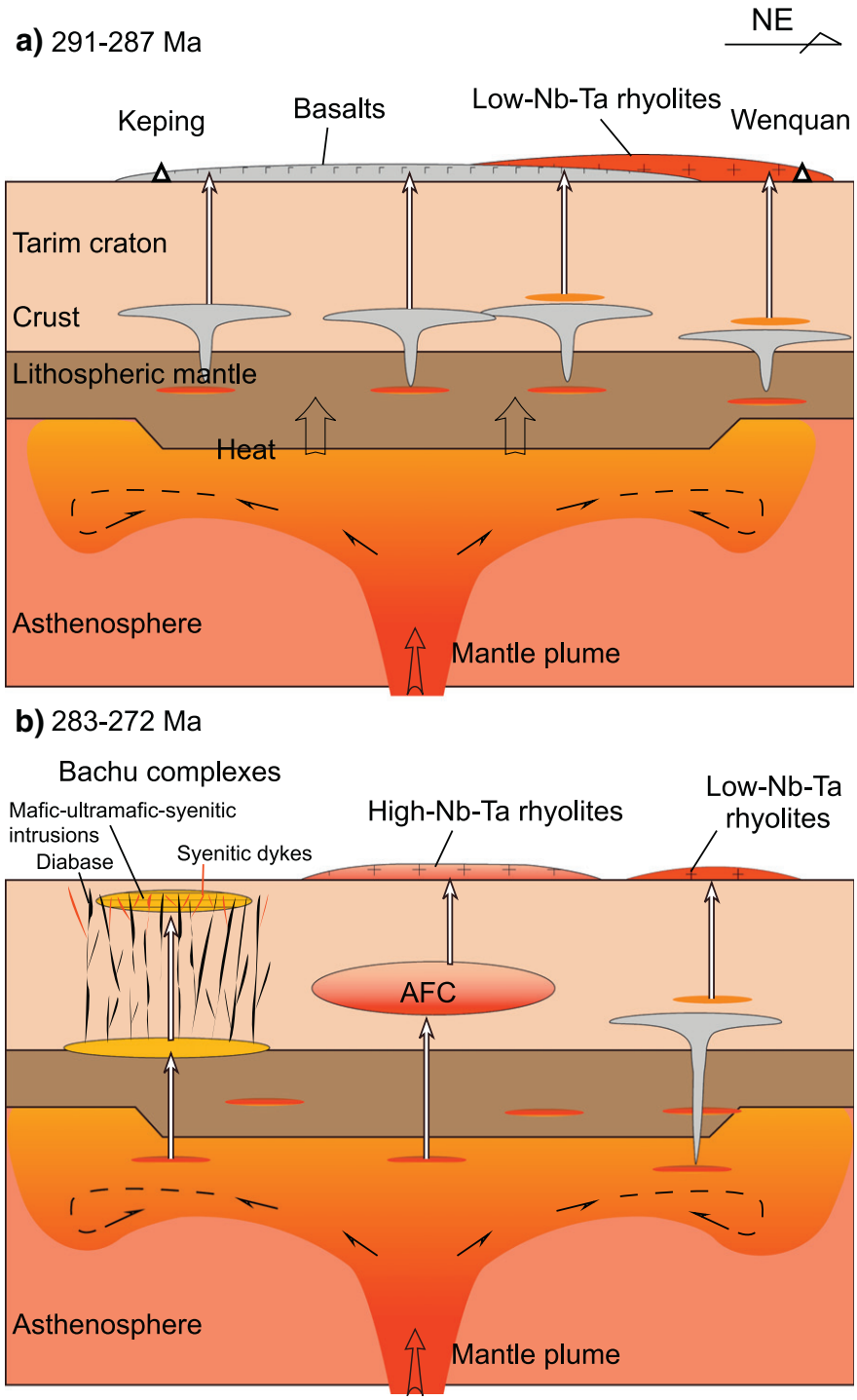

Fig. 10. A time-integrated Permian mantle plume model explaining petrogenesis of rhyolites from the Tarim Large Igneous Province. The low Nb–Ta rhyolites are indirect products of crustal anatexis induced by impact of mantle plume. The high Nb–Ta rhyolites are fractionation products of mantle plume-derived OIB-like magma with incorporation of continental crust via assimilation–fractionation crystallization process.

6. Conclusions

Two main types of rhyolites are recognized in the Tarim LIP in terms of their geochemical compositions. The low Nb–Ta rhyolites have two episodes of eruption. The first episode of eruption is closely associated to the ~290 Ma Tarim flood basalt volcanism and was likely formed by partial melting of ancient basement rocks. The high Nb–Ta rhyolites and their plutonic equivalents are associated with the second episode of the Tarim magmatism (~280 Ma). Their compositions are consistent with a derivation via assimilation–fractionation crystallization from an OIB-like mantle magma.

The evolution of the Tarim rhyolites mirrors the geodynamic processes in the Tarim LIP. At ~290 Ma, as a result of conductive heating from an incubating plume, the enriched lithospheric mantle melts to generate flood basaltic volcanism. The low Nb–Ta rhyolites were formed through crustal melting as a consequence of convective heating by underplated magmas. A relatively low magma generation rate is not favorable for the development of large magmatic chambers and accounts

for the general absence of mafic–ultramafic complexes and the high Nb–Ta rhyolites at this stage. At ~280 Ma, large magma chambers and plumbing systems were formed due to increasing magma supply rate during decompression melting of the mantle plume. This led to the formation of mafic–ultramafic–felsic association of which the high Nb–Ta rhyolites are one of the constituents.

Acknowledgments

We are grateful to Jin-Hui Yang, Ying Liu, Guang-Qian Hu, Jin-Long Ma, Xi-Rong Liang and Xiang-Lin Tu for the arrangement of experimental work. We thank Andrew Kerr, J. Gregory Shellnutt and an anonymous referee for their constructive reviews. This paper was supported by research grants from the National Basic Research Program of China (2011CB808906), GIGCAS 135 project (Y234051001) and the National Natural Science Foundation of China (41203009). The GIG publication is no 1837.

Appendix A. Supplementary data

Supplementary data to this article can be found online at http://dx.doi.org/10.1016/j.lithos.2014.02.007.

References

Allègre, C.J., Minster, J.F., 1978. Quantitative models of trace element behavior in magmatic processes. Earth and Planetary Science Letters 38, 1–25.
Annen, C., Sparks, R.S.J., 2002. Effects of repetitive emplacement of basaltic intrusions on thermal evolution and melt generation in the crust. Earth and Planetary Science Letters 203, 937–955.
Annen, C., Blundy, J.D., Sparks, R.S.J., 2006. The genesis of intermediate and silicic magmas in deep crustal hot zones. Journal of Petrology 47, 505–539.
Barbarin, B., 1999. A review of the relationships between granitoid types, their origins and their geodynamic environments. Lithos 46, 605–626.
Black, L.P., Kamo, S.L., Williams, I.S., Mundil, R., Davis, D.W., Korsch, R.J., Foudoulis, C., 2003. The application of SHRIMP to Phanerozoic geochronology: a critical appraisal of four zircon standards. Chemical Geology 200, 171–188.
Black, L.P., Kamo, S.L., Allen, C.M., Davis, D.W., Aleinikoff, J.N., Valley, J.W., Mundil, R., Campbell, I.H., Korsch, R.J., Williams, I.S., Foudoulis, C., 2004. Improved $^{206}Pb/^{238}U$ microprobe geochronology by the monitoring of a trace-element-related matrix effect; SHRIMP, ID-TIMS, ELA-ICP-MS and oxygen isotope documentation for a series of zircon standards. Chemical Geology 205, 115–140.
Bohrson, W.A., Spera, F.J., 2001. Energy-constrained open-system magmatic processes II: application of energy-constrained assimilation–fractional crystallization (EC-AFC) model to magmatic systems. Journal of Petrology 42, 1019–1041.
Bryan, S., 2007. Silicic large igneous provinces. Episodes 30, 20–31.
Bryan, S.E., Ernst, R.E., 2008. Revised definition of Large Igneous Provinces (LIPs). Earth-Science Reviews 86, 175–202.
Bryan, S.E., Constantine, A.E., Stephens, C.J., Ewart, A., Schönc, R.W., Parianos, J., 1997. Early Cretaceous volcano–sedimentary successions along the eastern Australian continental margin: implications for the break-up of eastern Gondwana. Earth and Planetary Science Letters 153, 85–102.
Bryan, S.E., Riley, T.R., Jerram, D.A., Stephens, C.J., Leat, P.T., 2002. Silicic volcanism: an undervalued component of large igneous provinces and volcanic rifted margins. Geological Society of America Special Papers 362, 97–118.
Cao, X.F., Lu, X.B., Liu, S.T., Zhang, P., Gao, X., Chen, C., Mo, Y.L., 2011. LA-ICP-MS zircon dating, geochemistry, petrogenesis and tectonic implications of the Dapingliang Neoproterozoic granites at Kuluketage block, NW China. Precambrian Research 186, 205–219.
Chen, Y.B., Hu, A.Q., Zhang, G.X., Zhang, Q.F., 2000. Precambrian basement age and characteristics of Southwestern Tianshan: zircon U Pb geochronology and Nd Sr isotopic compositions. Acta Petrologica Sinica 16, 91–98 (in Chinese with English Abstract).
Chen, H.L., Yang, S.F., Wang, Q.H., Luo, J.C., Jia, C.Z., Wei, G.Q., Li, Z.L., He, G.Y., Hu, A.P., 2006. Sedimentary response to the Early–Mid Permian basaltic magmatism in the Tarim plate. Geology in China 33, 545–552 (in Chinese with English abstract).
Chen, M.M., Tian, W., Zhang, Z.L., Pan, W.Q., Song, Y., 2010. Geochronology of the Permian basic-intermediate-acidic magma suite from Tarim, Northwest China and its geological implications. Acta Petrologica Sinica 26, 559–572 (in Chinese with English abstract).
Coble, M.A., Mahood, G.A., 2012. Initial impingement of the Yellowstone plume located by widespread silicic volcanism contemporaneous with Columbia River flood basalts. Geology 40, 655–658.
Coffin, M.F., Eldholm, O., 1994. Large igneous provinces: crustal structure, dimensions, and external consequences. Reviews of Geophysics 32, 1–36.
Collins, W., Beams, S., White, A., Chappell, B., 1982. Nature and origin of A-type granites with particular reference to southeastern Australia. Contributions to Mineralogy and Petrology 80, 189–200.
Creaser, R.A., Price, R.C., Wormald, R.J., 1991. A-type granites revisited: assessment of a residual-source model. Geology 19, 163–166.
Ewart, A., Milner, S.C., Armstrong, R.A., Duncan, A.R., 1998. Etendeka volcanism of the Goboboseb Mountains and Messum igneous complex, Namibia. Part II: voluminous quartz latite volcanism of the Awahab magma system. Journal of Petrology 39, 227–253.
Ewart, A., Marsh, J.S., Milner, S.C., Duncan, A.R., Kamber, B.S., Armstrong, R.A., 2004. Petrology and geochemistry of Early Cretaceous bimodal continental flood volcanism of the NW Etendeka, Namibia. Part 2: Characteristics and petrogenesis of the high-Ti latite and high-Ti and low-Ti voluminous quartz latite eruptives. Journal of Petrology 45, 107–138.
Frindt, S., Trumbull, R.B., Romer, R.L., 2004. Petrogenesis of the Gross Spitzkoppe topaz granite, central western Namibia: a geochemical and Nd–Sr–Pb isotope study. Chemical Geology 206, 43–71.
Frost, C.D., Bell, J.M., Frost, B.R., Chamberlain, K.R., 2001. Crustal growth by magmatic underplating: isotopic evidence from the northern Sherman batholith. Geology 29, 515–518.
Ge, R.F., Zhu, W.B., Wu, H.L., Zheng, B.H., Zhu, X.Q., He, J.W., 2012. The Paleozoic northern margin of the Tarim Craton: passive or active? Lithos 142, 1–15.
Goto, A., Tatsumi, Y., 1996. Quantitative analysis of rock samples by an X-ray fluorescence spectrometer (II). The Rigaku Journal 13, 20–39.
Haapala, I., Frindt, S., Kandara, J., 2007. Cretaceous Gross Spitzkoppe and Klein Spitzkoppe stocks in Namibia: Topaz-bearing A-type granites related to continental rifting and mantle plume. Lithos 97, 174–192.
Harris, C., Marsh, J.S., Milner, S.C., 1999. Petrology of the alkaline core of the Messum igneous complex, Namibia: evidence for the progressively decreasing effect of crustal contamination. Journal of Petrology 40, 1377–1397.
Hu, A.Q., Jahn, B.-m., Zhang, G., Chen, Y., Zhang, Q., 2000. Crustal evolution and Phanerozoic crustal growth in northern Xinjiang: Nd isotopic evidence. Part I. Isotopic characterization of basement rocks. Tectonophysics 328, 15–51.
Huang, H.-Q., Li, X.-H., Li, W.-X., Li, Z.-X., 2011. Formation of high $\delta^{18}O$ fayalite-bearing A-type granite by high-temperature melting of granulitic metasedimentary rocks, southern China. Geology 39, 903–906.
Huppert, H.E., Sparks, R.S.J., 1988. The generation of granitic magmas by intrusion of basalt into continental crust. Journal of Petrology 29, 599–624.
Irmis, R.B., Mundil, R., Martz, J.W., Parker, W.G., 2011. High-resolution U–Pb ages from the Upper Triassic Chinle Formation (New Mexico, USA) support a diachronous rise of dinosaurs. Earth and Planetary Science Letters 309, 258–267.
Jahn, B.-m., Wu, F., Chen, B., 2000. Massive granitoid generation in Central Asia: Nd isotope evidence and implication for continental growth in the Phanerozoic. Episodes 23, 82–92.
Jiang, C.Y., Jiang, H.B., Ye, S.F., Xia, M.Z., Lu, D.X., 2005. Petrochemical characteristics, Nd, Sr, Pb isotopic compositions and petrogenesis of Permian Dike Swarm, Kuruktag Region, Xinjiang. Acta Geologica Sinica 79, 823–833 (in Chinese with English abstract).
King, P.L., White, A.J.R., Chappell, B.W., Allen, C.M., 1997. Characterization and origin of aluminous A-type granites from the Lachlan Fold Belt, Southeastern Australia. Journal of Petrology 38, 371–391.
Li, X.-H., Li, Z.-X., Wingate, M.T.D., Chung, S.-L., Liu, Y., Lin, G.-C., Li, W.-X., 2006. Geochemistry of the 755 Ma Mundine Well dyke swarm, northwestern Australia: part of a Neoproterozoic mantle superplume beneath Rodinia? Precambrian Research 146, 1–15.
Li, X.-H., Long, W.-G., Li, Q.-L., Liu, Y., Zheng, Y.-F., Yang, Y.-H., Chamberlain, K.R., Wan, D.-F., Guo, C.-H., Wang, X.-C., Tao, H., 2010. Penglai zircon megacrysts: a potential new working reference material for microbeam determination of Hf–O isotopes and U–Pb age. Geostandards and Geoanalytical Research 34, 117–134.
Li, Z.L., Chen, H., Song, B., Li, Y., Yang, S., Yu, X., 2011. Temporal evolution of the Permian large igneous province in Tarim Basin in northwestern China. Journal of Asian Earth Sciences 42, 917–927.
Li, Z.L., Li, Y.Q., Chen, H.L., Santosh, M., Yang, S.F., Xu, Y.G., Langmuir, C.H., Chen, Z.X., Yu, X., Zou, S.Y., 2012. Hf isotopic characteristics of the Tarim Permian large igneous province rocks of NW China: implication for the magmatic source and evolution. Journal of Asian Earth Sciences 49, 191–202.
Li, X.-H., Tang, G.-Q., Gong, B., Yang, Y.-H., Hou, K.-J., Hu, Z.-C., Li, Q.-L., Liu, Y., Li, W.-X., 2013. Qinghu zircon: a working reference for microbeam analysis of U–Pb age and Hf and O isotopes. Chinese Science Bulletin 58. http://dx.doi.org/10.1007/s11434-013-5932-x.
Liang, X.R., Wei, G.J., Li, X.H., Liu, Y., 2003. Precise measurement of $^{143}Nd/^{144}Nd$ and Sm/Nd ratios using multiple collectors inductively coupled plasma mass spectrometer (MC-ICPMS). Geochimica 32, 91–96 (in Chinese with English abstract).
Liu, Y., Liu, H.C., Li, X.H., 1996. Simultaneous and precise determination of 40 trace elements in rock samples using ICP-MS. Geochimica 25, 552–558 (in Chinese with English abstract).
Liu, H.-Q., Xu, Y.-G., He, -B., 2013. Implications from zircon-saturation temperatures and lithological assemblages for Early Permian thermal anomaly in northwest China. Lithos 182–183, 125–133.
Long, X.P., Yuan, C., Sun, M., Zhao, G.C., Xiao, W.J., Wang, Y.J., Yang, Y.H., Hu, A.Q., 2010. Archean crustal evolution of the northern Tarim craton, NW China: zircon U–Pb and Hf isotopic constraints. Precambrian Research 180, 272–284.
Long, X.P., Yuan, C., Sun, M., Kröner, A., Zhao, G., Wilde, S., Hu, A., 2011. Reworking of the Tarim Craton by underplating of mantle plume-derived magmas: evidence from Neoproterozoic granitoids in the Kuluketage area, NW China. Precambrian Research 187, 1–14.
Ludwig, K.R., 2003. ISOPLOT 3: a geochronological toolkit for Microsoft excel. Berkeley Geochronology Centre Special Publication 4, 74.
Ma, X.X., Shu, L., Jahn, B.-M., Zhu, W., Faure, M., 2012. Precambrian tectonic evolution of Central Tianshan, NW China: constraints from U–Pb dating and in situ Hf isotopic analysis of detrital zircons. Precambrian Research 222–223, 450–473.

Mattinson, J.M., 2005. Zircon U–Pb chemical abrasion ("CA-TIMS") method: combined annealing and multi-step partial dissolution analysis for improved precision and accuracy of zircon ages. Chemical Geology 220, 47–66.
Mingram, B., Trumbull, R.B., Littman, S., Gerstenberger, H., 2000. A petrogenetic study of anorogenic felsic magmatism in the Cretaceous Paresis ring complex, Namibia: evidence for mixing of crust and mantle-derived components. Lithos 54, 1–22.
Mundil, R., Ludwig, K.R., Metcalfe, I., Renne, P.R., 2004. Age and Timing of the Permian Mass Extinctions: U/Pb Dating of Closed-System Zircons. Science 305, 1760–1763.
Nash, B.P., Perkins, M.E., Christensen, J.N., Lee, D.-C., Halliday, A.N., 2006. The Yellowstone hotspot in space and time: Nd and Hf isotopes in silicic magmas. Earth and Planetary Science Letters 247, 143–156.
Rudnick, R.L., Gao, S., 2003. 3.01 — composition of the continental crust. Treatise on Geochemistry. Pergamon, Oxford, pp. 1–64.
Schmitt, A.K., Emmermann, R., Trumbull, R.B., BÜHN, B., Henjes-Kunst, F., 2000. Petrogenesis and $^{40}Ar/^{39}Ar$ geochronology of the Brandberg complex, Namibia: evidence for a major mantle contribution in metaluminous and peralkaline granites. Journal of Petrology 41, 1207–1239.
ShangGuan, S.M., Tian, W., Li, X.H., Guan, P., Pan, M., Chen, M.M., Pan, W.Q., 2011. SIMS Zircon U–Pb age of a rhyolite layer from the Halahatang Area, Northern Tarim, NW China: constraint on the eruption age of major pulse of Tarim flood basalt. Acta Scientiarum Naturalium Universitatis Pekinensis 47, 561–564 (in Chinese with English abstract).
Shellnutt, J.G., Jahn, B.M., 2010. Formation of the Late Permian Panzhihua plutonic–hypabyssal–volcanic igneous complex: implications for the genesis of Fe–Ti oxide deposits and A-type granites of SW China. Earth and Planetary Science Letters 289, 509–519.
Shellnutt, J.G., Zhou, M.-F., 2007. Permian peralkaline, peraluminous and metaluminous A-type granites in the Panxi district, SW China: their relationship to the Emeishan mantle plume. Chemical Geology 243, 286–316.
Shellnutt, J.G., Bhat, G.M., Wang, K.-L., Brookfield, M.E., Dostal, J., Jahn, B.-M., 2012. Origin of the silicic rocks of the Early Permian Panjal Traps, Kashmir, India. Chemical Geology 334, 154–170.
Skjerlie, K.P., Johnston, A.D., 1993. Fluid-absent melting behavior of an F-rich tonalitic gneiss at mid-crustal pressures: implications for the generation of anorogenic granites. Journal of Petrology 34, 785–815.
Sparks, R.S.J., Meyer, P., Sigurdsson, H., 1980. Density variation amongst mid-ocean ridge basalts: implications for magma mixing and the scarcity of primitive lavas. Earth and Planetary Science Letters 46, 419–430.
Spera, F.J., Bohrson, W.A., 2001. Energy-constrained open-system magmatic processes I: general model and Energy-Constrained Assimilation and Fractional Crystallization (EC-AFC) formulation. Journal of Petrology 42, 999–1018.
Sun, S.S., McDonough, W.F., 1989. Chemical and isotopic systematics of oceanic basalts: implications for mantle composition and processes. Geological Society, London, Special Publications 42, 313–345.
Tian, W., Campbell, I., Allen, C., Guan, P., Pan, W., Chen, M., Yu, H., Zhu, W., 2010. The Tarim picrite–basalt–rhyolite suite, a Permian flood basalt from northwest China with contrasting rhyolites produced by fractional crystallization and anatexis. Contributions to Mineralogy and Petrology 160, 407–425.
Trumbull, R.B., Harris, C., Frindt, S., Wigand, M., 2004. Oxygen and neodymium isotope evidence for source diversity in Cretaceous anorogenic granites from Namibia and implications for A-type granite genesis. Lithos 73, 21–40.
Turner, S.P., Foden, J.D., Morrison, R.S., 1992. Derivation of some A-type magmas by fractionation of basaltic magma: an example from the Padthaway Ridge, South Australia. Lithos 28, 151–179.
Valley, J.W., Lackey, J.S., Cavosie, A.J., Clechenko, C.C., Spicuzza, M.J., Basei, M.A.S., Bindeman, I.N., Ferreira, V.P., Sial, A.N., King, E.M., Peck, W.H., Sinha, A.K., Wei, C.S., 2005. 4.4 billion years of crustal maturation: oxygen isotope ratios of magmatic zircon. Contributions to Mineralogy and Petrology 150, 561–580.
Wang, C., Liu, L., Che, Z., He, S., Li, R., Yang, W., Cao, Y., Zhu, X., 2009. Zircon U–Pb and Hf isotopic from the east segment of Tiekelike Tectonic Belt: constrains on the timing of Precambrian basement at the Southwestern Margin of Tarim, China. Dizhi Xuebao 83, 1647–1656 (in Chinese with English abstract).
Watson, E.B., Harrison, T.M., 1983. Zircon saturation revisited: temperature and composition effects in a variety of crustal magma types. Earth and Planetary Science Letters 64, 295–304.
Wei, X., Xu, Y.G., 2011. Petrogenesis of Xiaohaizi syenite complex from Bachu area, Tarim. Acta Petrologica Sinica 27, 2984–3004 (in Chinese with English abstract).
Wei, G.J., Liang, X.R., Li, X.H., Liu, Y., 2002. Precise measurement of Sr isotopic composition of liquid and solid base using (LP)MC ICPMS. Geochimica 31, 295–299.
Wei, X., Xu, Y.G., Feng, X.Y., Zhao, J.X., 2014. Plume-lithosphere interaction in the generation of the Tarim large igneous province, NW China: geochronological and geochemical constraints. American Journal of Science 314, 314–356.
Wu, F.Y., Yang, Y.H., Xie, L.W., Yang, J.H., Xu, P., 2006. Hf isotopic compositions of the standard zircons and baddeleyites used in U–Pb geochronology. Chemical Geology 234, 105–126.
Wu, G.H., Zhang, C.Z., Wang, H., Liu, Y.K., Li, J.J., 2009. Zircon SHRIMP U–Pb age of granodiorite of the Tacan 1 well in the central Tarim basin, China. Geological Bulletin of China 28, 568–571 (in Chinese with English abstract).
Xinjiang Bureau of Geology and Mineral Resources (XJBGMR), 1993. Regional Geology of Xinjiang Uygur Autonomous Region, Series 1. Geological Publishing House, Beijing (762 pp.).
Xu, B., Jian, P., Zheng, H., Zou, H., Zhang, L., Liu, D., 2005. U–Pb zircon geochronology and geochemistry of Neoproterozoic volcanic rocks in the Tarim Block of northwest China: implications for the breakup of Rodinia supercontinent and Neoproterozoic glaciations. Precambrian Research 136, 107–123.
Xu, Y.G., Luo, Z.Y., Huang, X.L., He, B., Xiao, L., Xie, L.W., Shi, Y.R., 2008. Zircon U–Pb and Hf isotope constraints on crustal melting associated with the Emeishan mantle plume. Geochimica et Cosmochimica Acta 72, 3084–3104.
Xu, Y.-G., Chung, S.-L., Shao, H., He, B., 2010. Silicic magmas from the Emeishan large igneous province, Southwest China: petrogenesis and their link with the end-Guadalupian biological crisis. Lithos 119, 47–60.
Xu, Y.G., He, B., Luo, Z.Y., Liu, H.Q., 2013. Study on Mantle Plume and Large Igneous Provinces in China: an overview and perspectives. Bulletin of Mineralogy, Petrology and Geochemistry 32, 25–39 (in Chinese with English abstract).
Yang, S.-F., Li, Z.-L., Chen, H.-L., Chen, W., Yu, X., 2006a. $^{40}Ar–^{39}Ar$ dating of basalts from Tarim Basin, NW China and its implication to a Permian thermal tectonic event. Journal of Zhejiang University — Science A 7, 320–324.
Yang, S.F., Li, Z.L., Chen, H.L., Xiao, W.J., Yu, X., Lin, X.B., Shi, X.G., 2006b. Discovery of a Permian quartz syenitic porphyritic dyke from the Tarim basin and its tectonic implications. Acta Petrologica Sinica 26, 1405–1412 (in Chinese with English abstract).
Yang, S.-F., Li, Z., Chen, H., Santosh, M., Dong, C.-W., Yu, X., 2007. Permian bimodal dyke of Tarim Basin, NW China: geochemical characteristics and tectonic implications. Gondwana Research 12, 113–120.
Yu, J.C., Mo, X.X., Dong, G.C., Yu, X.H., Xing, F.C., Li, Y., Huang, X.K., 2011a. Felsic volcanic rocks from northern Tarim, NW China: zircon U–Pb dating and geochemical characteristics. Acta Petrologica Sinica 27, 2184–2194 (in Chinese with English abstract).
Yu, X., Yang, S.-F., Chen, H.-L., Chen, Z.-Q., Li, Z.-L., Batt, G.E., Li, Y.-Q., 2011b. Permian flood basalts from the Tarim Basin, Northwest China: SHRIMP zircon U–Pb dating and geochemical characteristics. Gondwana Research 20, 485–497.
Zhang, C.-L., Li, X.-H., Li, Z.-X., Lu, S.-N., Ye, H.-M., Li, H.-M., 2007a. Neoproterozoic ultramafic–mafic–carbonatite complex and granitoids in Quruqtagh of northeastern Tarim Block, western China: geochronology, geochemistry and tectonic implications. Precambrian Research 152, 149–169.
Zhang, C.-L., Li, Z.-X., Li, X.-H., Yu, H.-F., Ye, H.-M., 2007b. An early Paleoproterozoic high-K intrusive complex in southwestern Tarim Block, NW China: age, geochemistry, and tectonic implications. Gondwana Research 12, 101–112.
Zhang, C.L., Li, Z.X., Li, X.H., Ye, H.M., 2009. Neoproterozoic mafic dyke swarms at the northern margin of the Tarim Block, NW China: age, geochemistry, petrogenesis and tectonic implications. Journal of Asian Earth Sciences 35, 167–179.
Zhang, C.L., Xu, Y.G., Li, Z.X., Wang, H.Y., Ye, H.M., 2010. Diverse Permian magmatism in the Tarim Block, NW China: genetically linked to the Permian Tarim mantle plume? Lithos 119, 537–552.
Zhang, C.-L., Zou, H.-B., Wang, H.-Y., Li, H.-K., Ye, H.-M., 2012. Multiple phases of the Neoproterozoic igneous activity in Quruqtagh of the northeastern Tarim Block, NW China: interaction between plate subduction and mantle plume? Precambrian Research 222–223, 488–502.
Zhong, H., Zhu, W.-G., Chu, Z.-Y., He, D.-F., Song, X.-Y., 2007. Shrimp U–Pb zircon geochronology, geochemistry, and Nd–Sr isotopic study of contrasting granites in the Emeishan large igneous province, SW China. Chemical Geology 236, 112–133.
Zhong, H., Campbell, I.H., Zhu, W.-G., Allen, C.M., Hu, R.-Z., Xie, L.-W., He, D.-F., 2011. Timing and source constraints on the relationship between mafic and felsic intrusions in the Emeishan large igneous province. Geochimica et Cosmochimica Acta 75, 1374–1395.
Zhou, M.F., Zhao, J.H., Jiang, C.Y., Gao, J.F., Wang, W., Yang, S.H., 2009. OIB-like, heterogeneous mantle sources of Permian basaltic magmatism in the western Tarim Basin, NW China: implications for a possible Permian large igneous province. Lithos 113, 583–594.